A halo model for cosmological Lyman-limit systems

Tom Theuns [1]★ and T. K. Chan [1,2]

[1]*Institute for Computational Cosmology, Department of Physics, Durham University, South Road, Durham DH1 3LE, UK*
[2]*Department of Astronomy and Astrophysics, the University of Chicago, Chicago, IL 60637, USA*

ABSTRACT

We present an analytical model for cosmological Lyman-limit systems (LLS) that successfully reproduces the observed evolution of the mean free path ($\lambda_{\rm eff}$) of ionizing photons. The evolution of the co-moving mean free path is predominantly a consequence of the changing meta galactic photoionization rate and the increase with cosmic time of the minimum mass below which haloes lose their gas due to photoheating. In the model, Lyman-limit absorption is caused by highly ionized gas in the outskirt of dark matter haloes. We exploit the association with haloes to compute statistical properties of $\lambda_{\rm eff}$ and of the bias, b, of LLS. The latter increases from $b \sim 1.5 \rightarrow 2.6$ from redshifts $z = 2 \rightarrow 6$. Combined with the rapid increase with redshift of the bias of the haloes that host a quasar, the model predicts a rapid drop in the value of $\lambda_{\rm eff}$ when *measured* in quasar spectra from $z = 5 \rightarrow 6$, whereas the *actual* value of $\lambda_{\rm eff}$ falls more smoothly. We derive an expression for the effective optical depth due to Lyman limit absorption as a function of wavelength and show that it depends sensitively on the poorly constrained number density of LLS as a function of column density. The optical depth drops below unity for all wavelengths below a redshift of ~ 2.5 which is therefore the epoch when the Universe first became transparent to ionizing photons.

Key words: radiative transfer – intergalactic medium – quasars: absorption lines – diffuse radiation.

1 INTRODUCTION

Hydrogen in the intergalactic medium (hereafter IGM) is so highly ionized that it does not produce a significant Gunn–Peterson trough (Gunn & Peterson 1965) in quasar spectra below a redshift of $z \sim 6$ (Fan et al. 2006). At higher redshifts, several independent observations suggest that the IGM may be significantly neutral. These include a detection of a damping wing in the spectra of $z > 7$ quasars (Mortlock et al. 2011; Davies et al. 2018) as well as other observations (e.g. Mason et al. 2018). The measurement of the Thompson-optical depth to the cosmic microwave background from free electrons also suggest that the Universe transitioned from mostly neutral to mostly ionized around $z \sim 7.5$ (Planck Collaboration et al. 2020). For reviews on the physics of the IGM and its connection to reionization, see e.g. Meiksin (2009) or McQuinn (2016), and for a more observational perspective, see e.g. Rauch (1998).

Even when the Universe is highly ionized on average, the remaining neutral hydrogen is sufficiently abundant to limit the distance that a typical ionizing photon can travel from its source before being absorbed. This distance can be quantified either by the attenuation length $\lambda_{\rm eff}$, defined below in equation (16), or the 'mean free path'. The relation between these quantities is examined in more detail in Appendix A. The attenuation length and the emissivity of ionizing sources together determine the amplitude of the ionizing background (e.g. Haardt & Madau 1996; Miralda-Escudé 2003; Faucher-Giguère et al. 2009; McQuinn, Oh & Faucher-Giguère 2011; Haardt & Madau 2012).

The absorbers of ionizing photons are usually characterised in terms of their neutral hydrogen column density, $N_{\rm HI}$, and are labeled as 'Lyman α forest' ($N_{\rm HI} < 10^{17.2}$ cm^{-2}), Lyman-limit systems (LLS's, $10^{17.2}$ cm$^{-2} \leq N_{\rm HI} < 10^{20.3}$ cm^{-2}), and damped Lyman α absorbers (DLA's, $N_{\rm HI} \geq 10^{20.3}$ cm^{-2}, see e.g. Rauch 1998). The optical depth of an ionizing photon with energy of 1 Rydberg is unity at $N_{\rm HI} = 10^{17.2}$ cm^{-2}, whereas the Lyman α line shows an obvious damping wing above a column density of $N_{\rm HI} = 10^{20.3}$ cm^{-2} – hence the labels. It is also common parlance to refer to absorbers with column density just below $10^{17.2}$ cm^{-2} as sub-LLS's, and those close to but below the DLA threshold as super-LLS's or sub-DLA's.

The column-density distribution function (hereafter CDDF), is the number density of absorbers with a given value of $N_{\rm HI}$ (per unit co-moving path length, to be defined below), and the normalization and shape of this function sets $\lambda_{\rm eff}$. Sub-LLS's and super-LLS's together mostly determine the value of $\lambda_{\rm eff}$, because the numerous Lyman α forest absorbers just have too low a column density to contribute significantly to $\lambda_{\rm eff}$, whereas the strongly absorbing DLA's are simply too rare. Unfortunately, it is difficult to measure accurately the column density of lines in the important range of 10^{16}–10^{20} cm^{-2} because the whole Lyman-series of absorption lines associated with the absorber is partially or completely saturated. Estimates of $\lambda_{\rm eff}$ then require extrapolating the CDDF in the LLS range, *i.e.* just that range of the CDDF that is the most important for accurately determining $\lambda_{\rm eff}$ (e.g. Faucher-Giguère et al. 2009; Haardt & Madau 2012).

Prochaska, Worseck & O'Meara (2009) suggested an alternative method for measuring $\lambda_{\rm eff}$, namely stacking quasar transmission spectra in bins of emission redshift and measuring the decrease in transmission caused by the ionization edge of the hydrogen atom

★ E-mail: tom.theuns@durham.ac.uk

– *i.e.* the reduction in transmission[1] of photons with energies $h\nu \geq 13.6 \mathrm{eV}$ (see also Fumagalli et al. 2013; O'Meara et al. 2013; Worseck et al. 2014; Becker et al. 2021). The measured value of λ_{eff} decreases rapidly with increasing z, approximately $\propto (1 + z)^{-\eta}$ with $\eta \approx 5.4$, over the redshift range $z = 2.3 \rightarrow 5.5$ (Worseck et al. 2014). This is much faster than would be the case if the absorbers had constant co-moving density and a constant proper cross-section, which would yield $\lambda_{\mathrm{eff}} \propto (1 + z)^{-3}$, demonstrating that the absorbers evolve. Given that the (co-moving) number density of absorbers presumably *increases* with cosmic time as structure grows, and that the intrinsic sizes of the absorbers presumably also grow with time, with both effects tending to *reduce* λ_{eff}, one might naively expect that λ_{eff} evolves *slower* than $(1 + z)^{-3}$ – which is exactly opposite from what is observed. Prochaska, O'Meara & Worseck (2010) discuss several possible reasons for this unexpected evolution, settling on the suggestion that it must be that absorbers become more highly ionized with decreasing z.

Becker et al. (2021) use the method of Prochaska, Worseck & O'Meara (2009) to measure λ_{eff} in a set of $z \sim 6$ quasars. Accounting for the radiation of the quasar itself – the proximity effect – they infer a sharp drop in λ_{eff} from $z = 5 \rightarrow 6$, much faster than an extrapolation of the $\propto (1 + z)^{-\eta}$ would predict. They claim that this rapid change signals the transition from an ionized to a mostly neutral IGM, and hence claim that their measurements are probing the tail-end of the epoch of reionization (see also Gaikwad et al. 2023).

Numerical models to predict the evolution of λ_{eff} are challenging, requiring radiative transfer (hereafter RT) at high resolution to capture the transition from ionized to neutral gas with increasing density in a computational volume that is large enough to sample the relatively rare strong absorbers that set λ_{eff}. Altay et al. (2011) and McQuinn, Oh & Faucher-Giguère (2011) both post-processed simulations with RT, showing that they can reproduce the observed CDDF, including the transition from Lyman α forest to DLA's. These papers show that the CDDF evolves relatively slowly, in agreement with observations (see also Rahmati et al. 2013). Altay et al. (2013) further show that these predictions are insensitive to the uncertainties in the modelling caused by *galaxy* formation (*i.e.* the implementation of feedback from massive stars and quasars), which only affects the CDDF at high column-densities, $N_{\mathrm{HI}} \geq 10^{21} \mathrm{cm}^{-2}$, that have little effect on λ_{eff}. All modellers agree that cold gas, accreting on to haloes, is the dominant contributor to LLS's (e.g. Altay et al. 2011; Faucher-Giguère & Kereš 2011; Fumagalli et al. 2011; van de Voort et al. 2012; Yajima, Choi & Nagamine 2012; Rahmati et al. 2013). Analytical models for the evolution of absorbers, sometimes augmented with observational constraints or numerical models, are also discussed by Erkal (2015) and Muñoz et al. (2016), and we will contrast our approach and results with theirs below.

A flurry of recent papers used simulations that include radiative transfer performed either on the fly or in post-processing to investigate the claim by Becker et al. (2021) that λ_{eff} drops sharply from $z = 5 \rightarrow 6$ (e.g. D'Aloisio et al. 2020; Keating et al. 2020; Cain et al. 2021; Garaldi et al. 2022; Gaikwad et al. 2023). The authors attribute the drop to this redshift range probing the tail-end of reionization. We will return to this issue in Section 3.2.

In this paper, we present an analytical model for the CDDF in the LLS and DLA range, making the assumption that (strong) absorption lines are caused by gas in haloes. The model of absorbers and their connection to λ_{eff} are presented in Section 2. Section 3 discusses

clustering of absorbers and the impact of bias on λ_{eff}. We also show how the statistical properties of the attenuation relate to clustering of haloes. Section 4 exploits the model to compute the wavelength dependence of the optical depth, resulting in a new model for the combined effect of many LLS on the mean transmission. Section 5 summarizes our results. We use the Planck Collaboration et al. (2016) values of cosmological parameters (final column of their table 4), Hubble parameter $h = 0.673$, baryon and matter density in units of the critical density of $\Omega_{\mathrm{b}} = 0.02230/h^2$ and $\Omega_{\mathrm{m}} = (0.1188 + 0.02230)/h^2$, a Helium abundance by mass of $Y = 0.24531$, and when applicable apply the high-z approximation for the Hubble constant at redshift z, $H(z) = H_0 \, \Omega_m^{1/2} \, (1 + z)^{3/2}$, with H_0 the Hubble constant at $z = 0$.

2 THE ATTENUATION LENGTH IN THE HALO MODEL

We begin this section by briefly reviewing the relation between the attenuation length, λ_{eff}, and the column density distribution function ($f(N_{\mathrm{H}}$, hereafter CDDF). We then extend the model of Theuns (2021) of DLA's to the lower column density LLS (Section 2.2), and use the resulting CDDF to derive the evolution of λ_{eff} which we compare to observations. We infer the main drivers of the evolution of λ_{eff} by varying the parameters that determine the CDDF (Section 2.3). We finish this section by comparing to the observed evolution of LLS's (Appendix B).

2.1 Relating λ_{eff} to the CDDF

Absorption of ionizing photons in the clumpy Universe occurs predominantly in approximately discrete 'absorbers' with a range of neutral hydrogen column densities, N_{HI}. Provided that these absorbers are Poisson distributed along a sight line (*i.e.*, provided we neglect any spatial correlations of absorbers: we account for clustering later on), the effective optical depth, τ_{eff}, per unit proper sight line distance, dl, at the Lyman limit, is (e.g. Paresce, McKee & Bowyer 1980; Meiksin & Madau 1993)

$$\frac{d\tau_{\mathrm{eff}}}{dl} = \int_0^\infty \frac{d^2 N}{dl \, dN_{\mathrm{HI}}} \left[1 - \exp(-\tau) \right] dN_{\mathrm{HI}}. \tag{1}$$

Here, N is the number of absorbers with column density N_{HI} per unit proper distance dl and $\tau = \sigma_{\mathrm{th}} N_{\mathrm{HI}}$ is the optical depth of an absorber; σ_{th} is the photoionization cross section at the Lyman limit. We will be more careful about the wavelength dependence of this relation later on.

The attenuation length is usually expressed as a proper distance. To expose better the underlying physics, it is useful to separate the contributions to the evolution of λ_{eff} that result from the expansion of the Universe and those that result from changes in the intrinsic properties of the absorbers. To enable this, Bahcall & Peebles (1969) defined the dimensionless co-moving path length, dX, as

$$dX \equiv \frac{H_0 (1 + z)^2}{H(z)} \, dz \equiv \frac{H_0 (1 + z)^3}{c} \, dl. \tag{2}$$

We note that dX is not simply the co-moving analogue of the proper path length dl. Combining the above relations yields

$$\frac{d\tau_{\mathrm{eff}}}{dX}(z) = \int_0^\infty f(N_{\mathrm{HI}}; z) \left[1 - \exp(-\tau) \right] dN_{\mathrm{HI}}, \tag{3}$$

where

$$f(N_{\mathrm{HI}}; z) \equiv \frac{d^2 N}{dX \, dN_{\mathrm{HI}}}(z), \tag{4}$$

---

[1] After correction for the reduction in transmission caused by the Lyman series of absorption lines, and accounting for other observational effects.

is now the number N of absorbers with a given column density per dX, *i.e.* the CDDF at redshift z.

The intensity of a beam of photons with frequency[2] ν_{th} travelling a co-moving path length dX will be attenuated by a factor $\exp(-\tau_{eff})$ on average. Setting $\tau_{eff} = 1$ in equation (3) defines the *attenuation length*, X_{eff},

$$X_{eff}(z) = \left\{ \int_0^\infty f(N_{H\,I}; z) \left[1 - \exp(-\tau)\right] dN_{H\,I} \right\}^{-1}. \qquad (5)$$

Any evolution of X_{eff} is due to the evolution of the CDDF, *i.e.* due to the evolution of the absorbers, rather than simply due to the expansion of the Universe.

Finally, the proper attenuation length, λ_{eff}, is related to X_{eff} by

$$\lambda_{eff} = \frac{c}{H_0 (1+z)^3} X_{eff}. \qquad (6)$$

The quantity λ_{eff} is sometimes referred to as mean free path. However, λ_{eff} and mean free path are different characterizations of absorption, and are generally not numerically equal, as we demonstrate in Appendix A

We continue by briefly reviewing the model of Theuns (2021) for strong $_{H\,I}$ absorbers, which we extend to lower values of the column density to compute the evolution of the CDDF and hence that of the attenuation length.

2.2 A model for the CDDF and its evolution

The model for strong H I absorbers by Theuns (2021, hereafter TT21, see also Erkal 2015) is based on the following two main approximations:

(i) Gas in haloes is spherically symmetrically distributed around the halo's centre of mass with a power-law density profile, $\rho(R) \propto R^{-2}$.

(ii) This gas is in photoionization equilibrium with the ionising background, and the neutral fraction can be estimated using approximate radiative transfer of ionizing photons penetrating radially inwards.

Spherical symmetry is clearly an approximation and it would be interesting to investigate how sensitive the model's predictions depend on this approximation.

In more detail, we assume the gas density profile to be[3]

$$n_{H}(R) = n_{H,h} \times \left(\frac{R_h}{R} \right)^2, \qquad (7)$$

Here, $n_{H}(R)$ is the hydrogen density by number at distance R from the centre of the halo, R_h is the virial radius of that halo, and $n_{H,h}$ is the density at R_h ($n_{H,h} = 200 f_{gas} \langle n_H \rangle /3$, with $\langle n_H \rangle$ the cosmic mean hydrogen density and f_{gas}, which is of order unity, the gas fraction at R_h in units of the cosmic mean). All these variables are in proper units. Assuming further that this halo is illuminated by an ionizing background characterized by a photoionization rate Γ_0, TT21 performs simplified radiative transfer to compute the neutral fraction, $x \equiv n_{H\,I}/n_H$ as a function of radius, assuming the gas is

isothermal at a temperature of $T = 10^4$ K. Calculating numerically the optical depth τ at radius R due to neutral gas between R and R_h yields the factor $\exp(-\tau)$ by which the photoionization rate at R is suppressed compared to its value at R_h. As τ increases, the neutral fraction rises rapidly once $\tau \geq 1$, and the gas transitions from highly ionized to mostly neutral.

In this paper, we extend TT21's model in two ways:

(1) we extrapolate the profile of equation (7) to values $>R_h$,
(2) we no longer assume that the gas is isothermal at a temperature of $T = 10^4$ K.

In practice, we extrapolate equation (6) out to $R = 8 R_h$. This extrapolation allows us to compute the number of absorbers at column densities far below that of DLA's, and we will show that the predicted number of such absorbers agrees fairly well with observations. The reason to make changes to the gas temperature as well is as follows. At lower densities where the gas is highly ionized, the gas temperature is closer to $T \sim 1.5 \times 10^4$ K (e.g. Schaye et al. 2000) at the redshifts of interest (*i.e.* $z = 2 \to 6$), and hence we would like to use this more realistic value for T. Choosing this higher temperature changes the neutral fraction due to the T-dependence of the recombination rate, at higher density it further changes the neutral fraction due to collisional ionization. To avoid that our self-shielded gas is affected by collisional ionizations, we want to keep the temperature of this gas at $T = 10^4$ K. We therefore interpolate T from 1.5×10^4 K at $\tau < 1$ to $T = 10^4$ K at $\tau \geq 1.5$. Given that these changes are relatively minor, we continue to refer to this improved model as 'TT21'.

We show below that the LLS's that set λ_{eff} are mostly highly ionized, and so even neglecting any self-shielding has little impact on our results. Given this, we make an even more simplified model in this paper which assumes that gas in LLS's is optically thin. The motivation for making this approximation is two-fold: (i) it dramatically simplifies the equations, and (ii) the attenuation length is nearly identical to that of the more accurate model. The simpler analytical expressions greatly clarify the relation between the evolution of X_{eff} and that of haloes. The reason for (ii) is that most of the absorption is due to LLS which occur in highly ionized gas that is well described by the approximate model. The approximation does *not* capture the transition from LLS's to DLA's. We will refer to the more accurate model as 'TT21' and to the model that makes the optically thin approximation as 'the optically thin' model.

The neutral fraction of the gas with the density profile of equation (7) can be computed analytically in the optically thin model. This also allows us to obtain an analytical expression for the column density along a sight line at impact parameter b,

$$N_{H\,I}(b) = N_{H\,I,h} \times \left(\frac{R_h}{b} \right)^3$$

$$N_{H\,I,h} \equiv \frac{2\alpha_B}{\Gamma_0} n_{H,h}^2 R_h \int_0^\infty \frac{dq}{(1+q^2)^2}$$

$$= 10^{15.5} \, cm^{-2} \left(\frac{1+z}{4} \right)^5 \left(\frac{M_h}{10^{10} M_\odot} \right)^{1/3}$$

$$\times \left(\frac{f_{gas}}{0.6} \right)^2 \left(\frac{\alpha_B(T)}{\alpha_B(1.5 \times 10^4 K)} \right) \left(\frac{\Gamma_0}{10^{-12} s^{-1}} \right)^{-1}. \qquad (8)$$

Here, $\alpha_B(T)$ is the case-B recombination coefficient, T is the temperature of the gas, and M_h is the virial mass of the halo. The value of $N_{H\,I,h}$ assumes that the $1/R^2$ profile of the halo extends to infinity, *i.e.* there is a (relatively small) contribution to $N_{H\,I}$ from gas outside the halo.

---

[2]Where $h\nu_{th} = 1$ Ryd is the binding energy of $_{H\,I}$. We discuss the frequency dependence in more detail in section 4. (From the context it should be clear when h is Planck's constant and when it refers to the Hubble parameter.)

[3]The model neglects the ~ 10 per cent effect of helium. It is straightforward to generate the model described here for a different exponent of the radial profile, which may be a better fit to profiles measured in simulations, in particular at higher $z \gtrsim 6$.

The column-density-weighted neutral fraction of the gas along a sight line is

$$\langle x \rangle = \frac{\int_0^\infty x\, n_{\mathrm{H\,I}}\, \mathrm{d}l}{\int_0^\infty n_{\mathrm{H\,I}}\, \mathrm{d}l} = \frac{3 x_h}{4} \left(\frac{N_{\mathrm{H\,I}}}{N_{\mathrm{H,h}}} \right)^{2/3}, \tag{9}$$

where $x_{\mathrm{h}} = \alpha_B n_{\mathrm{H,h}}/\Gamma_0$ is the neutral fraction at R_{h}, and l is the path length. For $z = 3$ and $\Gamma_0 = 10^{-12}\,\mathrm{s}^{-1}$, $x_{\mathrm{h}} \approx 10^{-4}$, which means that $\langle x \rangle < x_m$ provided that $N_{\mathrm{H\,I}} < N_{\mathrm{H,h}}\,(x_m/x_h)^{3/2}$ or $N_{\mathrm{H\,I}} \lesssim 500\, N_{\mathrm{H,h}}$ taking $x_m = 10^{-2}$. Comparing to equation (8) then shows that up to columns of order a few times $10^{18}\,\mathrm{cm}^{-2}$, the absorbing gas is indeed highly ionized, $x < 10^{-2}$, hence making the optically thin approximation is likely justified for LLS. We will show later that absorbers with column densities around this value are the dominant contributors to the attenuation length. This explains why the optically thin model gives very similar values for X_{eff} to the more detailed model of TT21.

The cross-section σ for which a halo of mass M_{h} yields a column density higher than a given value of $N_{\mathrm{H\,I}}$ is

$$\sigma(> N_{\mathrm{H\,I}}) = \pi b^2(> N_{\mathrm{H\,I}}) = \pi R_h^2 \times \left(\frac{N_{\mathrm{H\,I,h}}}{N_{\mathrm{H\,I}}} \right)^{2/3}. \tag{10}$$

Some previous models of absorbers (e.g. Fumagalli et al. 2013; Erkal 2015) set $\sigma = f_{\mathrm{cov}}\, \pi R_h^2$, where f_{cov} is a dimensionless 'covering factor'. In our model, equation (8) shows that *even in a spherically symmetric model*, f_{cov} depends on M_{h}, T, and Γ_0, and rather strongly on redshift. We[4] now follow TT21 by defining the function $g(M_{\mathrm{h}}, N_{\mathrm{H\,I}}, z)$ as the number of absorbers with a given column density per unit co-moving path length $\mathrm{d}X$ due to haloes of mass M_{h}. TT21 shows that this function is proportional to the derivative of the cross-section with respect to $N_{\mathrm{H\,I}}$ times the halo mass function, $\mathrm{d}n/\mathrm{d}\log M_{\mathrm{h}}$,

$$\begin{aligned} g(M_{\mathrm{h}}, N_{\mathrm{H\,I}}, z) &\equiv \frac{\mathrm{d}^3 N}{\mathrm{d}N_{\mathrm{H\,I}}\, \mathrm{d}\log M_{\mathrm{h}}\, \mathrm{d}X} \\ &= -\frac{c}{H_0} \frac{\mathrm{d}n(M_{\mathrm{h}}, z)}{\mathrm{d}\log M_{\mathrm{h}}} \frac{\mathrm{d}\sigma(M_{\mathrm{h}}, > N_{\mathrm{H\,I}}, z)}{\mathrm{d}N_{\mathrm{H\,I}}} \\ &= \frac{2c}{3 H_0} \frac{\mathrm{d}n(M_{\mathrm{h}}, z)}{\mathrm{d}\log M_{\mathrm{h}}} \frac{\pi R_h^2}{N_{\mathrm{H\,I,h}}} \left(\frac{N_{\mathrm{H\,I,h}}}{N_{\mathrm{H\,I}}} \right)^{5/3}. \end{aligned} \tag{11}$$

The halo mass function, $\mathrm{d}n/\mathrm{d}\log M_{\mathrm{h}}$, is the co-moving number density of haloes with mass M_{h} per dex in halo mass. The cross-section σ, on the other hand, is defined in *proper* units. Therefore the function g will only evolve if the halo mass function evolves in co-moving units, or if the absorbers themselves evolve in proper units, or both.

Integrating the function g over halo mass yields the CDDF,

$$f(N_{\mathrm{H\,I}}, z) = \int_{\log M_{\mathrm{crit}}(z)}^\infty g(M_h, N_{\mathrm{H\,I}}, z)\, \mathrm{d}\log M_h. \tag{12}$$

We note that the lower limit of the integral over halo mass in equation (12) is $\log M_{\mathrm{crit}}(z)$, where $M_{\mathrm{crit}}(z)$ is the mass below which haloes lose their gas when it is photoheated by the ionizing background. Obviously, such haloes will not host absorbers and hence will not contribute to the CDDF. In this paper, we use the fit by Okamoto, Gao & Theuns (2008) to evaluate $M_{\mathrm{crit}}(z)$. It might also be useful to limit the upper limit of integration in equation (12) since gas in sufficiently massive haloes is likely to be hot and collisionally ionized, rather than cold and neutral – and hence our model would be a poor description of gas in such haloes. Fortunately, such massive haloes are rare at the high redshifts $z \geq 2$ that we are mostly interested in, and the steep fall off of the mass function at high M_{h} implies that such haloes contribute negligibly in any case.

Table 1. Model parameters as a function of redshift, z. M_{crit} is the critical halo mass below which haloes lose their baryons, taken from Okamoto, Gao & Theuns (2008); f_c is the dimensionless variable entering equation (14).

z	$\log M_{\mathrm{crit}}\ (\mathrm{M}_\odot)$	f_c
0	9.82	0.94
1	9.57	0.98
2	9.35	0.87
3	8.99	0.77
4	8.71	0.65
5	8.42	0.55
6	8.19	0.46

Combining all what we found so far allows us to obtain the following analytical expression for the CDDF:

$$\begin{aligned} f(N_{\mathrm{H\,I}}, z) = 8.67 &\times 10^{-19}\mathrm{cm}^2\, \frac{f_{17.2}(z)}{\Gamma_{-12}^{2/3}(z)} \left(\frac{N_{\mathrm{H\,I}}}{10^{17.2}\mathrm{cm}^{-2}} \right)^{-5/3} \\ &\times \left(\frac{f_{\mathrm{gas}}}{0.6} \right)^{4/3} \left(\frac{\alpha_B(T)}{\alpha_B(1.5 \times 10^4 \mathrm{K})} \right)^{2/3}, \end{aligned} \tag{13}$$

where $f_{17.2}(z)$ is the dimensionless function

$$f_{17.2}(z) \equiv \frac{f_c(z)}{f_c(3)} \left(\frac{1+z}{4} \right)^{4/3},$$

$$\frac{f_c(z)}{\mathrm{cMpc}^3} \equiv \int_{\log M_{\mathrm{crit}}(z)}^\infty \frac{\mathrm{d}n(M_h, z)}{\mathrm{d}\log M_h} \left(\frac{M_h}{10^{10}\mathrm{M}_\odot} \right)^{8/9} \mathrm{d}\log M_h, \tag{14}$$

and $\Gamma_{-12} \equiv \Gamma_0/(10^{-12}\mathrm{s}^{-1})$; we note that the normalization $f_{17.2}(z = 3) = 1$ by construction. Equation (13) brings out the scaling of the CDDF with column density, $N_{\mathrm{H\,I}}$, IGM temperature, T, and photoionization rate, Γ_{-12}, with any additional redshift dependence encoded by $f_{17.2}(z)$. From now on we will set $f_{\mathrm{gas}} = 0.6$ and $T = 1.5 \times 10^4$ K, and drop them from the equations. If required, the interested reader can always resurrect them by replacing $f_{17.2} \to f_{17.2} \times (f_{\mathrm{gas}}/0.6)^{4/3} \times \left[\alpha_B(T)/\alpha_B(T = 1.5 \times 10^4 \mathrm{K}) \right]^{2/3}$.

The explicit redshift dependence of the CDDF is encoded by the function $f_{17.2}(z)$, which depends on $f_c(z)$. The latter dimensionless quantity is approximately[5] the mass in a volume of 1 cMpc^3 that is in haloes of mass $> M_{\mathrm{crit}}(z)$, divided by $10^{10}\,\mathrm{M}_\odot$. This quantity depends on z but is of order unity. The additional redshift dependence for $f_{17.2}$ of $\propto (1+z)^{4/3}$ arises from the z dependence of the relation between halo mass and virial radius. Values of M_{crit} and f_c as a function of redshift are given in Table 1. To compute the integral over mass, we used the COLOSSUS PYTHON package of Diemer (2018), selecting the implementation of the fit by Reed et al. (2007) of the halo mass function, $\mathrm{d}n/\mathrm{d}\log M_h$.

The analytical optically thin CDDF is a power-law in column density, $f \propto N_{\mathrm{H\,I}}^{-5/3}$ (see also TT21); the value of $-5/3$ for the exponent results from the assumed slope of the density profile of gas in haloes, $n_{\mathrm{H}}(R) \propto R^{-2}$. The model's dependence on $N_{\mathrm{H\,I}}$ agrees well with that of the observed CDDF which is also approximately a power law with slope -1.66 ± 0.01 at $\bar{z} = 2.99$ and -1.68 ± 0.02 at $\bar{z} = 3.48$ at column densities $\lesssim 10^{16}$ cm^{-2} (e.g. Kim et al. 2021). Faucher-Giguère et al. (2009) and Haardt & Madau (2012) provide more accurate fitting functions for the CDDF towards higher and lower N_{HI}.

Absorbers with column density $N_{\mathrm{H\,I}} \sim 10^{17.2}$ cm^{-2} and higher are particularly important for setting the opacity of the IGM to ionising

---

[4]The minus sign is, unfortunately, missing in TT21.

[5]It would be that fraction if the exponent of M_h in the integral were 1, rather than 8/9.
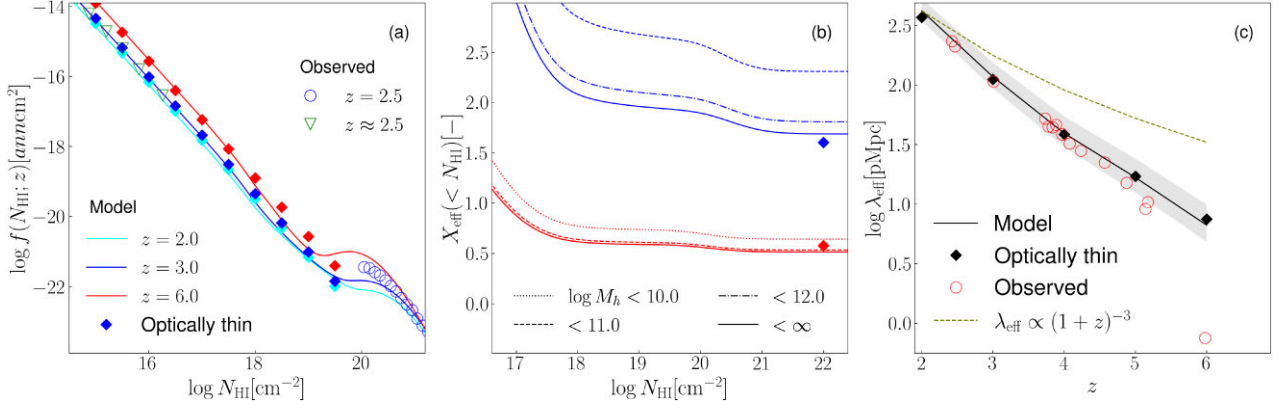
Figure 1. Evolution of – *left-hand panel*: the CDDF, $f(N_{\mathrm{H\,I}})$, *central panel:* attenuation length, X_{eff}, plotted cumulatively as a function of column density, *right-hand panel:* proper attenuation length λ_{eff}. *Solid lines* are from the model by Theuns (2021), with *cyan, blue,* and *red solid lines* corresponding to $z = 2, 3$, and 6, and the *black solid line* in the right-hand panel showing the evolution with z. *Solid diamonds* show the optically thin approximation at those same redshifts, with the CDDF in the left-hand panel computed using equation (12), the attenuation length computed using equation (5) (central panel), and the corresponding proper attenuation length computed using equation (2). In the central panel, the *solid curve* includes all halo masses, the *dotted* and *dashed* and *dotted–dashed* curves include haloes up to 10^{10}, 10^{11}, and 10^{12} $\mathrm{M_\odot}$ solar masses. In the right-hand panel, the *shaded area* corresponds to varying M_{crit} (equation (12) – the critical halo mass below which haloes lose their gas due to photoevaporation – by a factor of 4 around the central value taken from Okamoto, Gao & Theuns (2008). Both the optically thin expression (squares) and the results of the model of TT21 (solid lines) use the photoionization rate $\Gamma_0(z)$ from Haardt & Madau (2012), cosmological parameters from Planck Collaboration et al. (2016) and the critical mass from Okamoto, Gao & Theuns (2008). *Coloured empty symbols* are observations: in the *left-hand panel*, *blue open circles* are the data at $z \sim 2.5$ from Noterdaeme et al. (2012), *downward green triangles* are the $z \approx 2.5$ data from Rudie et al. (2013); the *open red circles* in the *right-hand panel* are the values taken from fig. 8 of Becker et al. (2021; see text for further details).

photons, unfortunately, the super-LLS range is also where it is very difficult to measure the slope of the CDDF. In addition, it is difficult to provide accurate measurements of the CDDF at higher redshifts. Given these observational limitations, it is useful to have an analytical model, such as the one presented here, which predicts the evolution of the CDDF and which agrees very well with the data where they are at their most reliable.

The model predicts that over a relatively large range in mass, haloes contribute about equally to the CDDF per dex in halo mass. The reason for this is at follows. At fixed $N_{\mathrm{H\,I}}$, the cross-section σ (above which the column density is higher than $N_{\mathrm{H\,I}}$) increases with halo mass $\propto M_h^{8/9}$, with equation (11) elucidating why: $\sigma \propto R_h^2 N_{\mathrm{H\,I,h}}^{2/3} \propto M_h^{8/9}$. We note, however, that the *number density* of haloes *decreases* with halo mass, approximately $\propto M_h^{-0.9}$ on the power-law part of the Press & Schechter (1974) halo mass function. As a consequence, all haloes with mass above the critical mass, $M_h > M_{\mathrm{crit}}$, but below the critical[6] Press–Schechter mass M_* contribute about equally to the amplitude of the CDDF, with those more massive than M_* contributing little.

The redshift evolution of the CDDF is a consequence of the following four effects: (i) the evolution of Γ_{-12}, (ii) the evolution of the halo mass function, (iii) the evolution of M_{crit}, and (iv) the explicit factor[7] $(1 + z)^{4/3}$ of equation (14). We examine the impact of the evolution of the CDDF on that of the attenuation length in the next section.

2.3 The evolution of the attenuation length

We can now combine equation (5) for X_{eff} in terms of the CDDF with equation (14) for the shape and evolution of the CDDF. We convert from column density, $N_{\mathrm{H\,I}}$, to optical depth, τ, using $\tau = \sigma_{\mathrm{th}} N_{\mathrm{H\,I}}$, where σ_{th} is the photoionization cross section at the Lyman limit ($h\nu_{\mathrm{th}}$

= 13.6 eV) and evaluate[8] the integral over optical depth between zero and infinity, $\int_0^\infty \tau^{-5/3} (1 - \exp(-\tau))\, \mathrm{d}\tau = 4.02$. This yields the following expression for the attenuation length[9],

$$X_{\mathrm{eff}}(z) = 1.80 \frac{\Gamma_{-12}^{2/3}(z)}{f_{17.2}(z)}; \tag{15}$$

for which the corresponding proper attenuation length is

$$\lambda_{\mathrm{eff}}(z) = \frac{c\, X_{\mathrm{eff}}(z)}{H_0\,(1+z)^3} = 126\,\mathrm{pMpc}\, \frac{\Gamma_{-12}^{2/3}(z)}{f_{17.2}(z)} \left(\frac{4}{1+z}\right)^3. \tag{16}$$

The results of our calculations so far are summarized in Fig. 1. The left-hand panel compares the CDDF as computed using the model by TT21 (solid lines) to the optically thin approximation of equation (12) at $z = 2$ (cyan line and cyan diamonds, respectively), $z = 3$ (blue line and blue diamonds) and $z = 6$ (red line and red diamonds). The full model includes self-shielding which causes the transition from $f(N_{\mathrm{H\,I}}) \propto N_{\mathrm{H\,I}}^{-5/3}$ in the highly ionized regime of LLS, to $f(N_{\mathrm{H\,I}}) \propto N_{\mathrm{H\,I}}^{-3}$ in the neutral DLA regime, with the characteristic 'knee' between the two power laws around $N_{\mathrm{H\,I}} = 10^{20}\,\mathrm{cm}^{-2}$ caused by the transition from ionized to neutral absorbers (Zheng & Miralda-Escudé 2002a; Erkal 2015; Theuns 2021). The optically thin model has the same slope and amplitude as the full model in the LLS regime. Errors on the observed data are comparable or smaller than the symbols, except for the $z \sim 6$ data point in the right-hand panel which we'll return to later.

---

[6]As in $\mathrm{d}n/\mathrm{d}\log M_h \propto M_h^{-\alpha_h} \exp(-M_h/M_*)$.

[7]This factor results from the redshift dependence of the M_h–R_h relation.

[8]Clearly it is incorrect to integrate from $\tau = 0$ to $\tau \to \infty$: we have not verified whether the optically thin model reproduces the CDDF in the regime of small τ that corresponds to the Lyman α forest, and the approximate expression for the CDDF is only valid for highly ionized absorbers and hence not applicable in the regime of DLA's. Fortunately, the contribution of very low-τ absorbers to X is negligible, and we will show that the contribution of high$-\tau$ absorbers depends on their number density but not on τ.

[9]Where we remind the reader that we have dropped the dependence on f_{gas} and T.
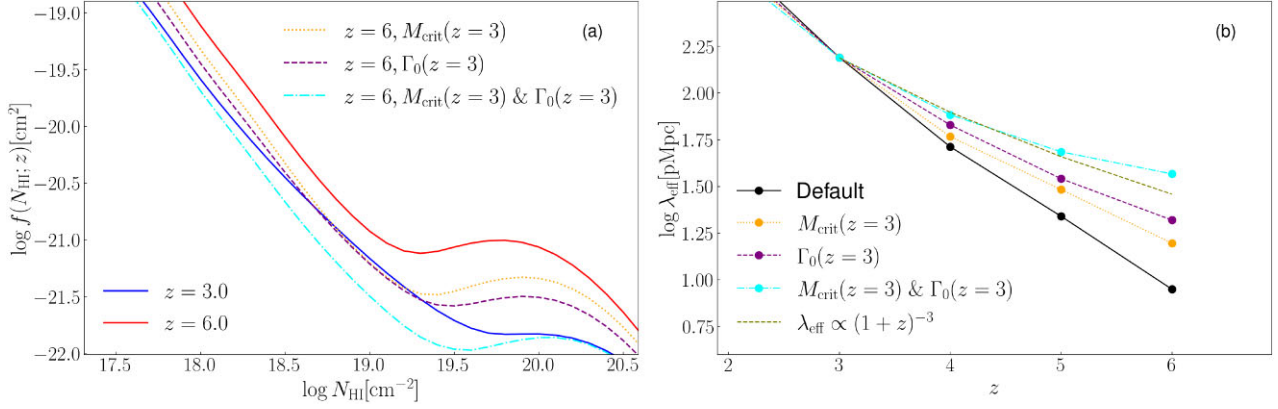
Figure 2. Similar to Fig. 1, with the *left-hand panel* showing the evolution of the CDDF, and the right-hand panel the evolution of the proper attenuation length, but this time also illustrating parameter dependencies. The default choice of parameters used in Fig. 1 is shown in *blue* and *red* in panel (a) for redshift $z = 3$ and 6, and black in panel (b). We then computed the CDDF at $z = 6$ but kept one or more parameters fixed at their value at $z = 3$. The *orange dotted line*, *purple dashed line*, and *cyan dot-dashed line* are the CDDF at $z = 6$, computed using the $z = 3$ value of M_{crit}, Γ_0, and both M_{crit} and Γ_0, respectively. This demonstrates that both parameters affect the evolution of the CDDF and when both are kept constant, there is hardly any remaining evolution left. Panel (b) shows the effect of these parameters on the evolution of λ_{eff}, where M_{crit}, Γ_0, and both M_{crit} are kept fixed at their $z = 3$ value for the *orange dotted line*, *purple dashed line*, and *cyan dotted–dashed line*. When both parameters are kept constant, λ_{eff} follows closely the evolution $\propto (1 + z)^{-3}$, shown as an *olive dashed line*. With M_{crit} and Γ_0 kept constant, the remaining evolution in λ_{eff} is mostly due to cosmological expansion, hence $\lambda_{eff} \propto (1 + z)^{-3}$. See the main text for further discussion.

The central panel plots the co-moving attenuation length $X_{eff}(< N_{HI})$ due to absorbers with column density less than N_{HI} in the TT21 model, for $z = 3$ and $z = 6$ (solid lines). The main contribution to X_{eff} is from absorbers in the relatively small column-density range of 10^{17} cm$^{-2} \leq N_{HI} \leq 10^{18}$ cm^{-2} at $z = 6$, and 10^{18} cm$^{-2} \leq N_{HI} \leq 10^{19}$ cm^{-2} at $z = 3$. The different line styles show the extent to which haloes of a given mass contribute, with dotted, dashed, and dotted–dashed lines showing the contribution due to haloes with mass less than 10^{10}, 10^{11}, and 10^{12} M$_\odot$. Haloes with mass $>10^{10}$ M$_\odot$ contribute little to X_{eff} at $z = 6$, but this increases to haloes with mass $>10^{11.5}$ M$_\odot$ by $z = 3$. The two diamonds show the value of $X_{eff}(z)$ obtained from the optically thin model using equation (15), with $z = 3$ and $z = 6$ shown as a blue and a red diamond. Clearly, this approximation captures the results of the more detailed model of TT21 very well.

The right-hand panel of Fig. 1 shows the evolution of the proper attenuation length. The solid black line is the evolution computed using the model of TT21. The grey shading shows the effect of varying the value of M_{crit} by factors 1/4 to 4, in order to illustrate how sensitive λ_{eff} is to this parameter. The black diamonds show the optically thin approximation, which captures the evolution of λ_{eff} very well. The solid red circles are the data points plotted in fig. 8 of Becker et al. (2021). The data are compiled from Prochaska, Worseck & O'Meara (2009), Fumagalli et al. (2013), O'Meara et al. (2013), Worseck et al. (2014), and Lusso et al. (2018), with the highest z point from Becker et al. (2021).

The model reproduces the observations well over the range $z = 2 \rightarrow 5$, and this is one of the main results of this paper. As a note of caution, we note that the value taken for f_{gas} affects λ_{eff}, yet our choice of taking $f_{gas} = 0.6$ is not particularly well motivated. We suspect that this parameter attempts to account for the fact that the neutral gas distribution in real absorbers is not spherically symmetric (see e.g. the analysis by Erkal 2015). TT21 use $f_{gas} = 0.5$ (rather than 0.6) in their model for DLA's, and hence a value of $f_{gas} \sim 0.6$ fits the CDDF all the way from LLS to DLA's at $z = 3$, as can be seen in the left-hand panel of the figure. Strikingly, the model does not show the dramatic decline in λ_{eff} suggested by the data from Becker et al. (2021) from $z = 5 \rightarrow 6$: we will return to this in Section 3.

The gold-dashed line in the right-hand panel of Fig. 1 shows the scaling $\propto (1 + z)^{-3}$. Both data and model evolve faster than this, implying that the absorbers either evolve in co-moving number density or proper size, or both. We examine the cause of the enhanced evolution in the model in more detail in Fig. 2 as follows: we redo the calculations but we keep the value of $M_{crit}(z)$ and $\Gamma_{-12}(z)$ constant and equal to their values at $z = 3$: this is the cyan curve in both panels. The left-hand panel shows that in this case, the $z = 6$ CDDF is almost identical to the $z = 3$ CDDF. We note that the main remaining difference is the evolution of the halo mass function, but that clearly has relatively little effect on the CDDF. The reason is that the halo mass function evolves relatively little below M_*, and haloes above M_* where the halo function does evolve rapidly contribute little to λ_{eff}.

The right-hand panel of Fig. 2 shows the effect of M_{crit} and Γ_{-12} separately. Both the evolution of M_{crit} and of Γ_{-12} contribute[10] to the evolution of the attenuation length, causing $X_{eff}(z)$ to increase with decreasing z. When these parameters are kept constant, X_{eff} evolves much less, and λ_{eff} evolves mostly due to cosmological expansion, $\lambda_{eff} \propto (1 + z)^{-3}$. This can be seen by the fact that the cyan line – for which M_{crit} and of Γ_{-12} both remain constant – falls almost on top of the $\lambda_{eff} \propto (1 + z)^{-3}$ scaling. The right-hand panel also shows that M_{crit} and Γ_{-12} contribute about equally to the evolution of X_{eff}. We plot the evolution of $X_{eff}(z)$ for the case of a constant amplitude of the ionization rate ($\Gamma_{-12}(z) = 1$) in Fig. 3.

Summarizing: the attenuation length X_{eff} evolves due to the evolution of M_{crit} and Γ_{-12}. M_{crit} is the critical mass below which haloes lose or cannot accrete gas. The evolution in M_{crit} is itself mostly caused by the fact that haloes cannot accrete gas if their virial temperature is lower than the temperature of the gas they attempt to accrete – and the virial temperature of a halo of given mass depends on z – hence the evolution. At lower z, M_{crit} is higher, and so a larger fraction of haloes no longer host the absorbers that limit X_{eff}, and hence X_{eff} increases. About equally important to the evolution of X_{eff} is that $\Gamma_{-12}(z)$ increases with decreasing z (from $z = 6 \rightarrow 2$), making
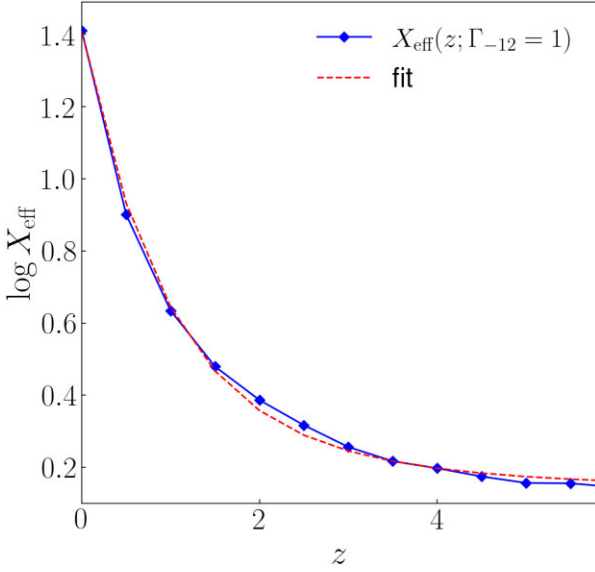
[10]See also Cain et al. (2023).

Figure 3. Evolution of the co-moving attenuation length, $X_{\rm eff}$, as given by equation (15) for the case of a constant amplitude of the ionization rate, $\Gamma_{-12}(z) = 1$. The fit shown by the *dashed red line* is $\log X_{\rm eff} = 1.38 + 24.2/(1 + z)^3$, which fits the model to better than 20 per cent.

the gas in the absorbers more highly ionized, which again increases $X_{\rm eff}$. Finally, we note that the co-moving number density of absorbers is proportional to the halo mass function, which, of course, *increases* with decreasing z. So, despite that the number density of absorber hosts increases, the net absorption they produce decreases and hence $X_{\rm eff}$ increases with cosmic time. We recall that the number density of haloes on the power-law tail of the Press–Schechter mass function does not actually evolve strongly.

The values of $X_{\rm eff}$ and $\lambda_{\rm eff}$ in the current model are set to a large extent by the number density of absorbers with $N_{\rm H\,I} \sim 10^{18}$ cm^{-2}. It is possible to directly count the number density of such strong absorbers in QSO spectra. We compare these predictions to observations in Appendix B. Because absorbers are associated with haloes in the current model, it is straightforward to infer the clustering of absorbers from the clustering of their host haloes. This is what we'll do next.

3 CLUSTERING OF ABSORBERS

In this section, we compute the bias (b) of absorbers as a function of their column density, finding that b is nearly independent of $N_{\rm H\,I}$. Somewhat surprisingly, we find that the bias of DLA's with $N_{\rm H\,I} \sim 10^{20.3}$ cm^{-2} is actually *lower* than that of LLS's and sub-LLS's. We use the bias-$N_{\rm H\,I}$ relation to investigate the impact of bias on $\lambda_{\rm eff}$ in Section 3.2, showing that the bias of quasars likely impacts the measured values of $\lambda_{\rm eff}$ significantly above $z \sim 5$. In Section 3.3, we use these findings to compute the probability distribution of $\tau_{\rm eff}$.

3.1 The bias of absorbers as a function of $N_{\rm H\,I}$

The bias of absorbers with a given hydrogen column density at redshift z follows from that of their host haloes as (TT21)

$$b_{N_{\rm H\,I}}(z) = \frac{\int_{\log M_{\rm crit}(z)}^{\infty} {\rm d} \log M_h \left\{ b_{M_h}(z) \times g(N_{\rm H\,I}, M_h, z) \right\}}{\int_{\log M_{\rm crit}(z)}^{\infty} {\rm d} \log M_h \left\{ g(N_{\rm H\,I}, M_h, z) \right\}}, \quad (17)$$

and the bias of absorbers with $N_{\rm H\,I} \geq 10^{17.2}$ cm^{-2} is

$$b_{\rm LLs}(z) = \frac{\int_{17.2}^{\infty} {\rm d} \log N_{\rm H\,I} \int_{\log M_{\rm crit}(z)}^{\infty} {\rm d} \log M_h \, \mathcal{F}_1(M_h, N_{\rm H\,I}, z)}{\int_{17.2}^{\infty} {\rm d} \log N_{\rm H\,I} \int_{\log M_{\rm crit}(z)}^{\infty} {\rm d} \log M_h \, \mathcal{F}_2(M_h, N_{\rm H\,I}, z)}$$
$$\mathcal{F}_1(M_h, N_{\rm H\,I}, z) = b_{M_h}(z) \, N_{\rm H\,I} \, g(N_{\rm H\,I}, M_h, z)$$
$$\mathcal{F}_2(M_h, N_{\rm H\,I}, z) = N_{\rm H\,I} \, g(N_{\rm H\,I}, M_h, z). \quad (18)$$

Here, $b_{M_h}(z)$ is the bias of a halo of virial mass $M_{\rm h}$ at redshift z, and column densities are assumed to be expressed in units of cm^{-2}.

The bias computed from equation (17) for absorbers with a given column density is plotted in panel (c) of Fig. 4, with colours indicating redshift. Below column densities of $\sim 10^{18.5}$ cm^{-2}, absorber bias is nearly independent of column density. At first somewhat surprising, we also find that the bias then *decreases* with increasing column density, until it reaches a minimum value for $N_{\rm H\,I} \sim 10^{20.3}$ cm^{-2}, after which the bias increases rapidly with increasing column density.

These trends can be understood by examining panel (a) of Fig. 4, where we plot the function $g(M_h, N_{\rm H\,I}, z)$ defined in equation (11) at a representative redshift[11] $z = 3$. Below a column density of $\sim 10^{18.5}$ cm^{-2}, the relative contribution of haloes as a function of mass varies little with column density because $g \propto N_{\rm H\,I}^{-5/3}$, independently of halo mass. Since all haloes contribute about equally to the number density of lines with a given $N_{\rm H\,I}$, it follows that the bias is independent of $N_{\rm H\,I}$.

However, the nature of absorbers changes from mostly ionized to mostly neutral at higher column densities, $N_{\rm H\,I} \sim 10^{19}$ cm^{-2}. This transition imprints the 'knee'-shaped feature in g and also in the CDDF (Zheng & Miralda-Escudé 2002b; Erkal 2015; Theuns 2021). Lower mass haloes transition from ionized to neutral at lower values of $N_{\rm H\,I}$ compared to higher mass haloes, as can be seen in panel (a) of Fig. 4. This results in a decrease in the absorber bias because more of these absorbers are associated with lower mass haloes – which themselves are less biased. Once $N_{\rm H\,I}$ is high enough so that most absorbers have made the transition from highly ionized to neutral, the bias increases rapidly with increasing $N_{\rm H\,I}$. This is because, in this regime, higher column densities are increasingly associated with more massive – and hence more highly biased – haloes – as is also apparent from panel (a) of Fig. 4.

The numerical value of the bias and its evolution with redshift can be understood by also examining panel (b) in Fig. 4, where we plot the halo bias, $b_{M_h}(z)$, computed using COLOSSUS (Diemer 2018). Panel (a) shows that haloes in the mass range 10^9–10^{11} M$_\odot$ contribute about equally to the CDDF at column densities $N_{\rm H\,I} \leq 10^{18.5}$ cm^{-2} at $z = 3$, resulting in a weighted bias of such absorbers of ~ 1.8, a bit less than that of haloes of mass 10^{11} M$_\odot$. With increasing redshift, the contribution of lower mass haloes increases compared to that of more massive haloes at a given value of $N_{\rm H\,I}$ – which would lower the bias. However, the bias of these same lower mass haloes *increases* rapidly with redshift. The net result of these opposing trends is an increase in the bias of absorbers with increasing z, as seen in panel (c).

Current measurements of the DLA bias yield values that range from $b = 1 \rightarrow 3$ (e.g. Alonso et al. 2018; Pérez-Ràfols et al. 2018, 2023). Given the strong dependence of b on $\log N_{\rm H\,I}$ and redshift in the model, a fair comparison between model and data requires careful modelling of the observational selection which we have not performed yet.

Finally, panel (c) also shows the bias of LLS's computed using equation (18) as filled black dots. With the function g decreasing

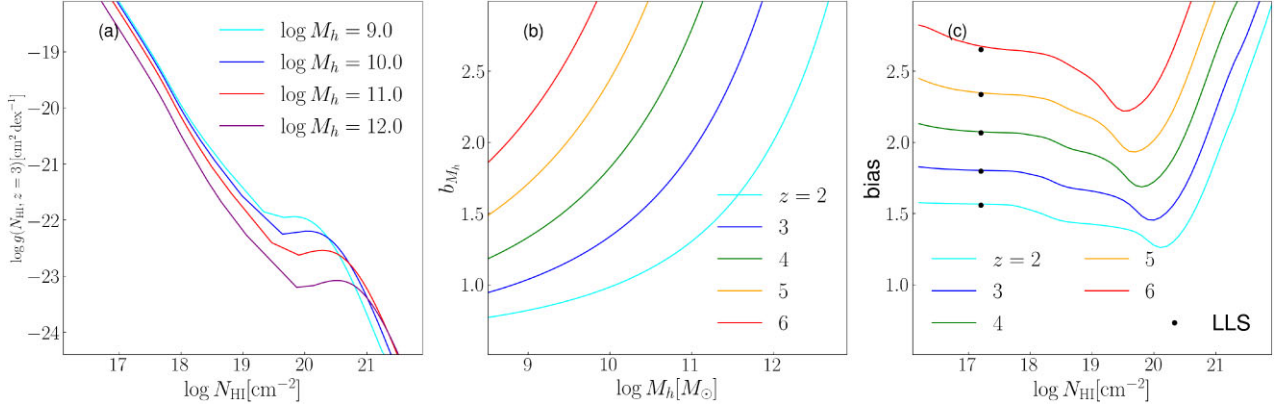[11] The trends with halo mass are similar at other redshifts.

Figure 4. Bias of absorption systems in the model of Theuns (2021), as computed from equation (17). *Panel (a):* contribution of haloes of a given mass to the CDDF at redshift $z = 3$, as given by equation (11). The somewhat artificial shape around $N_{\mathrm{H\,I}} \sim 10^{19}$ cm^{-2} is due to our interpolation of the temperature of the gas from $T = 15\,000$ K when optically thin to $T = 10^4$ K for $\tau \geq 1$. *Panel (b):* bias of haloes as a function of their mass, b_{M_h}, at different redshifts, as computed with COLOSSUS (Diemer 2018). Panel (c): Bias for lines of a given column density, $b_{N_{\mathrm{H\,I}}}$ from equation (17), for different redshifts; *black circles* show the bias for Lyman-limit systems, b_{LLs} from equation (18), for those same redshifts; these points are plotted at $N_{\mathrm{H\,I}} = 10^{17.2}$ cm^{-2}. The bias of LLS's (absorbers with $N_{\mathrm{H\,I}} \geq 10^{17.2}$ cm^{-2}) is very close to that of lines with a column density of $10^{17.2}$ cm^{-2}. Coloured lines in panel (a) correspond to different halo masses, and in panels (b) and (c) correspond to different redshifts, as per the legends. See text for discussion.

rapidly with increasing $N_{\mathrm{H\,I}}$, it is not surprising that the bias of LLS's is close to that of absorbers with $N_{\mathrm{H\,I}} = 10^{17.2}$ cm^{-2}. In the next section, we use the bias of absorbers to calculate the attenuation length of photons that themselves emanate from a biased region.

3.2 The impact of bias on the attenuation length

Up to now, we calculated the attenuation length λ_{eff} in the general IGM. However, in observations, λ_{eff} is measured from QSO spectra. Given that QSO's may well predominantly be hosted by massive haloes that are biased, particularly at higher redshifts, *observed* values of λ_{eff} are potentially biased. We can use the absorber bias determined in the previous section to examine the importance of both sources of bias (QSO and absorber) on the measured value of λ_{eff} as follows.

Consider absorbers with column density $N_{\mathrm{H\,I}}$, located at a proper distance between l and $l + \mathrm{d}l$ from a source (typically a QSO). The contribution of such absorbers to the effective optical depth at the Lyman limit towards that source is on average

$$\langle \mathrm{d}\tau_{\mathrm{eff}} \rangle = \langle N \rangle \left[1 - \exp(-\tau)\right]$$
$$\langle N \rangle = f(N_{\mathrm{H\,I}})\, \mathrm{d}N_{\mathrm{H\,I}} \frac{\mathrm{d}X}{\mathrm{d}l}\, \mathrm{d}l, \tag{19}$$

according to equation (3), where $\langle N \rangle$ is the average number of these absorbers and $\tau = \sigma_{\mathrm{th}} N_{\mathrm{H\,I}}$ is the optical depth of a single absorber at the Lyman limit; $\mathrm{d}X/\mathrm{d}l$ is given by equation (2). In the absence of clustering, $f(N_{\mathrm{H\,I}})$ is independent of l, and hence so is the average number of absorbers, $\langle N \rangle$.

With bias of both absorbers and source accounted for, $\langle N \rangle$ changes to[12]

$$\langle N \rangle = f(N_{\mathrm{H\,I}}) \left\{ 1 + b_S\, b_{N_{\mathrm{H\,I}}} \xi(l) \right\} \mathrm{d}N_{\mathrm{H\,I}} \frac{\mathrm{d}X}{\mathrm{d}l}\, \mathrm{d}l. \tag{20}$$

The factor $\left\{ 1 + b_S\, b_{N_{\mathrm{H\,I}}} \xi(l) \right\}$ accounts for linear bias between absorbers and source; $\xi(l)$ is the correlation function of the mass.

In the parlance of halo bias, we note that this accounts for the 'two-halo' term, *i.e.* the clustering of the haloes hosting absorber and source, rather than the fact that the host halo of the source may itself host an 'associated' absorber (which would be the 'one-halo' term, due to absorbers within the host galaxy of the QSO, associated with its own circumgalactic medium, its satellite galaxies or with Magellanic Stream-like features, say).

We now take advantage of the findings in the previous section that the bias of an absorber, $b_{N_{\mathrm{H\,I}}}$, is approximately independent of column density for the column densities below 10^{19} cm^{-2} that dominate the attenuation. Therefore, it is a good approximation to replace $b_{N_{\mathrm{H\,I}}} \to b_{\mathrm{LLS}}$. We can now compute the attenuation length when accounting for bias, $X_{\mathrm{b,eff}}$, in terms of its unbiased value, X_{eff}, by using equation (5),

$$\int_0^{X_{\mathrm{b,eff}}} [1 + b_S b_{\mathrm{LLS}} \xi(X)]\, \mathrm{d}X = X_{\mathrm{eff}}. \tag{21}$$

Since $b_{\mathrm{LLS}} > 1$ and b_S and ξ can be significantly larger than 1, $X_{\mathrm{b,eff}} < X_{\mathrm{eff}}$: since there are (possibly many) more absorbers close to the QSO per unit $\mathrm{d}X$ than in the general IGM, the attenuation length measured in the spectra of a QSO is generally shorter than its value in the general IGM.

An easy way to account for biasing is to define the dimensionless variable $\mathrm{d}Y$ by

$$\mathrm{d}Y \equiv [1 + b_S\, b_{\mathrm{LLS}}\, \xi(X)]\, \mathrm{d}X, \tag{22}$$

with boundary condition[13] $Y = 0$ for $X = 0$. The statistical properties of the effective optical depth out to X depends on Y, which we dub 'biased absorption length'. Using Y, rather than X, allows us to include the effects of the clustering of absorbers with sources of ionizing photons easily. The average number of absorbers that contribute to $\mathrm{d}\tau_{\mathrm{eff}}$ in a narrow interval of biased absorption length $[Y, Y + \mathrm{d}Y]$ from a source is then simply

$$\langle N(Y) \rangle = f(N_{\mathrm{H\,I}}) \mathrm{d}N_{\mathrm{H\,I}}\, \mathrm{d}Y, \tag{23}$$

---

[12]This assumes the linear halo bias model of Mo, van den Bosch & White (2010).

[13]ξ is usually expressed as a function of co-moving distance, $l(1 + z)$, but we find it more convenient to express ξ as a function of X.

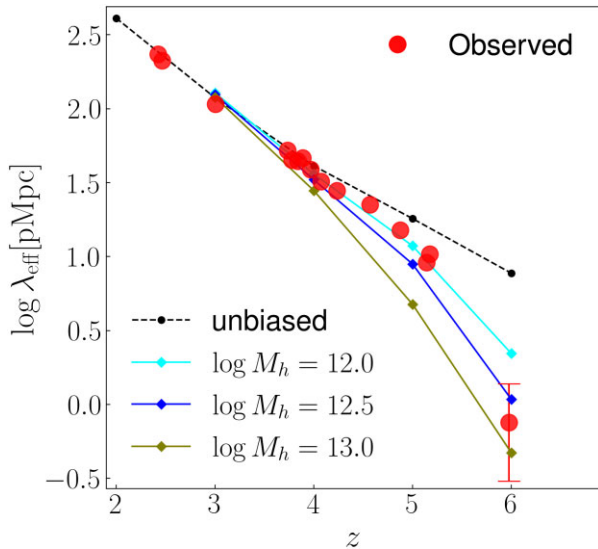**Figure 5.** Proper attenuation length $\lambda_{\rm eff}$ as a function of redshift, z. The *dashed black line* is the unbiased model repeated from Fig. 1 (where it was labelled 'model'). The other curves include the effects of the absorber and source bias from equation (21). The bias of Lyman-limit systems at redshift z is computed as in Section 3.1; the bias of the host halo of the QSO is computed for various halo masses $M_{\rm h}$ as indicated in the legend. *Red symbols* repeat the observational data from Fig. 1, with the $z = 6$ data point additionally displaying the uncertainty in the measured value of $\lambda_{\rm eff}$ taken from Becker et al. (2021).

and looks identical to the case where bias is neglected – except for the change of variables $X \to Y$.

We used the COLOSSUS PYTHON package of Diemer (2018) to compute the correlation function ξ at several redshifts, and then evaluated equation (21) to compute $X_{\rm b,eff}$ and $\lambda_{\rm b,eff}$, the attenuation lengths at the Lyman limit when accounting for bias; the results are shown in Fig. 5. As illustrative examples, we plot $\lambda_{\rm b,eff}$ when the bias of the source equals that of halos of mass 10^{12}, $10^{12.5}$, and 10^{13} $M_\odot$ (cyan, dark blue and olive line) with the bias of the absorbers as calculated in the previous section. In contrast, the unbiased case repeated from Fig. 1 is shown as a dashed black line. $\lambda_{\rm b,eff}$ decreases with increasing source bias (increasing halo mass), as expected. Around $z \sim 3$, even haloes of mass $10^{12.5}$ $M_\odot$ are not that strongly biased to make $\lambda_{\rm b,eff}$ differ significantly from $\lambda_{\rm eff}$. However, b_S for such haloes increases rapidly with increasing z (see e.g. the middle panel of Fig. 4), and at $z = 6$, $\lambda_{\rm b,eff} \ll \lambda_{\rm eff}$. QSO host halo masses of $\sim 10^{12.5}$ $M_\odot$ (dark blue line) bring the computed value of the attenuation length in better agreement with the data, and also reproduces the rapid decreases in the measured value of $\lambda_{\rm b,eff}$ towards $z = 6$. Values of $M_{\rm h} \sim 10^{12.5}$ $M_\odot$ are expected for the host halo masses of $z \sim 6$ QSO's (see de Beer et al. 2023; Zhang et al. 2023 and references therein, see also Bower et al. 2017 for a more general physical model for what sets the halo mass of bright AGN).

The sudden decrease in $\lambda_{\rm b,eff}$ from $z = 5 \to 6$ in our model is due to the rapid increase in bias of the host halo of the QSO in which $\lambda_{\rm b,eff}$ is measured (itself a consequence of the host halo mass being on the exponential part of halo mass function). Several recent papers instead investigate the possibility that this drop is because this redshift range probes the tail-end of reionization (e.g. D'Aloisio et al. 2020; Keating et al. 2020; Cain et al. 2021; Garaldi et al. 2022; Gaikwad et al. 2023). If this were correct, the drop might be due to a rapid change in the emissivity of ionizing photons and/or in the clumping factor of the IGM. Which interpretation is correct? We

first note that the number density of QSO's with 1450 Å magnitude brighter than -26 (*i.e.* comparable to those of the XQR-30 sample presented by Bosman et al. 2022 and used by Gaikwad et al. 2023) – is $\sim 10^{-9}$ cMpc^{-3}mag^{-1} at $z \sim 6$ (Onoue et al. 2017). This implies that even the largest simulation volume investigated in these papers (of order 160 cMpc^3) contains on average only $\sim 4 \times 10^{-3}$ QSO's as luminous (and hence plausibly as biased) as those observed. This illustrates the challenge of performing simulations that resolve the physically small absorbers in a simulation that is large enough to also contain the kind of background sources against which we detect them observationally. It also means that these papers cannot test the impact of bias discussed in this paper. Obviously, even if bias plays an important role, it is still possible that this redshift range probes the tail-end of reionization: the two explanations are not mutually exclusive.

3.3 The PDF of the biased attenuation length

We calculated the mean value of the biased attenuation length in the spectrum of a QSO in the previous section as an integral of $f(N_{\rm H\,I})$, where the CDDF is the *mean* number of absorbers with a given column density $N_{\rm H\,I}$ per dX. However, a given sight line may have slightly more or slightly fewer lines than that mean number. As a consequence, the effective optical depth of a given sight line with a given extent ΔX may be larger or smaller than the ensemble average. To quantify this, we compute in this section $\mathcal{P}(\tau_{\rm eff}|X)$ – the PDF of the effective optical depth for a sight line with a given co-moving path length X. Similarly, we defined and computed the co-moving attenuation length as that value of X for which $\tau_{\rm eff} = 1$. Accounting for variations in the number of absorbers along different sight lines, we can compute $\mathcal{P}(\tau_{\rm eff} = 1, X)$ – the probability that $\tau_{\rm eff} = 1$ for a given absorption path length. These PDF's may be useful when interpreting observations that are based on a relatively small number of independent sight lines. It is straightforward to account for bias in these calculations by using dY rather than dX, but we think that our analysis is easier to follow when we perform the calculation in terms of dX.

We will assume that the absorbers are *Poisson-distributed*, so that the probability $\mathcal{P}(N)$ for finding N absorbers in a region where the mean number is $\langle N \rangle$ is given by

$$\mathcal{P}(N) = \mathbb{P}(N|\langle N \rangle) \equiv \frac{\langle N \rangle^N \exp(-\langle N \rangle)}{N!}, \qquad (24)$$

where $\mathbb{P}(n|\mu)$ is the Poisson distribution with mean μ. In terms of the contribution of such absorbers to the effective optical depth, the PDF of d$\tau_{\rm eff}$ follows from that of N by a change of variables,

$$\mathcal{P}(\mathrm{d}\tau_{\rm eff}) = \mathbb{P}(N|\langle N \rangle) \frac{1}{1 - \exp(-\tau)}, \qquad (25)$$

with mean $\langle N \rangle (1 - \exp(-\tau))$ and dispersion $\langle N \rangle (1 - \exp(-\tau))^2$.

The total effective optical depth is obtained by integrating d$\tau_{\rm eff}$ over all column densities, but there is no simple relation between the Poisson statistics of the lines and the PDF of $\tau_{\rm eff}$. This is because a linear combination of Poisson distributed variables is not Poisson distributed (or indeed has any other simple PDF[14]). We can generate Poisson-distributed variables for all N's (*i.e.* absorbers with a given small range in column density) and sum $\tau_{\rm eff}$ in bins of d$N_{\rm H\,I}$ and dX, and compute the PDF of $\tau_{\rm eff}$ numerically. It is also possible to derive

---

[14]See *e.g.* Bohm & Zech (2014) for a discussion of such 'Compound Poisson distributions'.
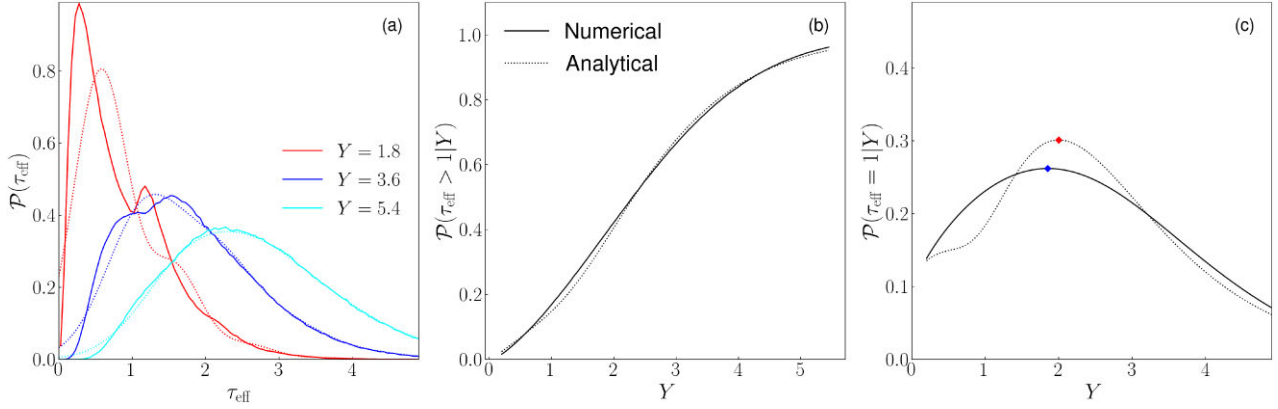
Figure 6. Statistics of the effective optical depth, $\tau_{\rm eff}$, and of the co-moving attenuation length, in terms of the (biased) absorption path length Y defined in equation (22). *Solid lines* are numerical results, obtained by generating Poisson-distributed absorbers numerically; *dashed lines* use the analytical approximation described in the text. *Left-hand panel:* Probability distribution of $\tau_{\rm eff}$ for the values Y indicated in the legend. The analytical expression is equation (C3). *Central panel:* fraction of paths that reach $\tau_{\rm eff} > 1$ within a length Y. The analytical expression is equation (C5). *Right-hand panel:* probability that a path with length Y reaches $\tau_{\rm eff} > 1$; the mean attenuation length is $Y_{\rm eff} = 1.8$. See text for further discussion.

an approximate analytical expression for the PDF. The approximation consists of assuming that absorbers with column below some value (we use $10^{17.2}$ cm^{-2}) are sufficiently numerous that we can apply the central limit theorem and take them to be Gaussian distributed. This allows the calculation of the PDF for 'low' τ absorbers. The stronger absorbers then all have transmission $\exp(-\tau) \approx 0$, and we can then also calculate their PDF. Summing the contribution of low and high τ absorbers yields the net PDF, see Appendix C for full details.

The results are illustrated in Fig. 6, where we plot them in terms of Y rather than X, with the change of variables accounting for the bias of absorbers and source. For illustrative purposes we assume a CDDF of the form of equation (13),

$$f(N_{\rm H\,I}) = 1.27 \times 10^{-18}\,{\rm cm}^2 \left(\frac{10^{17.2}\,{\rm cm}^{-2}}{N_{\rm H\,I}} \right)^{5/3}, \tag{26}$$

for which $Y_{\rm eff} = 1.8$. We draw Poisson distributed absorption lines from this CDDF in narrow bins of $N_{\rm H\,I}$, which allow us to compute $\tau_{\rm eff}$ for a given biased absorption distance Y. We can use this to compute the fraction of paths that reach $\tau_{\rm eff} > 1$ within a given value of Y, and the fraction of paths that reach $\tau_{\rm eff} > 1$ in a narrow interval dY around Y. These are shown as solid lines in panels (a)→(c). The corresponding analytical expressions, equations (C3), (C5), and (C6) derived in Appendix C are plotted with dashed lines.

When Y is small – the case $Y = 1.8$ (which is equal to the biased attenuation length) in panel (a) – the PDF of $\tau_{\rm eff}$ has two clear maxima, which correspond to 0 or 1 strong absorbers contributing to $\tau_{\rm eff}$ (there are further oscillations visible, due to 2 or more strong absorbers). Absorbers with $\tau \lesssim 10^{17.2}$ cm^{-2} are sufficiently rare when Y is small that approximating their PDF as Gaussian is not very accurate. This is the reason that the analytical model differs noticeably from the numerical calculation for small values of Y. As Y increases, such absorbers become more common and the approximation improves.

The analytical model reproduces rather well the fraction of paths that reach $\tau_{\rm eff} > 1$ within a given path length Y, as shown in panel (b). The derivative of this function with respect to Y is the probability that a given path reaches $\tau_{\rm eff} > 1$ in a small interval dY around Y, and is plotted in panel (c). The peak of the analytical approximation (red dot) is a bit narrower than that of the numerical result (blue dot), but the location of the maxima is very close. Both functions have a long tail to large values of Y, with the analytical approximation reproducing the numerical result well.

Note that the attenuation length in the case shown is $Y_{\rm eff} = 1.8$ - yet less than 30 per cent of sight lines with path length $Y = Y_{\rm eff}$ reach $\tau_{\rm eff} = 1$ because the distribution of $\mathcal{P}(\tau_{\rm eff} = 1, Y)$ around the mean is quite wide. This is of course because absorption is dominated by the rare, high column density absorbers.

4 A DIRECT MEASURE OF THE ATTENUATION LENGTH

An intervening absorber with column $N_{\rm H\,I} \geq 10^{17.2}$ cm^{-2} imprints an absorption edge in the spectrum of a quasar at wavelengths $\lambda \leq \lambda_{\rm th} \approx 912.1$ Å in the rest frame of the absorber. Because the photoionization cross-section falls $\propto \lambda^3$, the optical depth due to such an absorber decreases at lower λ. However, a second intervening absorber at lower redshift may introduce another absorption edge, which will increase the optical depth again. The total optical depth[15] below $\lambda_{\rm th}$ in the rest frame of the quasar is therefore a balance between the fall in τ of any individual LLS and the increase in τ due to the increase in the number of intervening LLS.

In this section, we use our expression for the evolution of the CDDF to compute $\tau_{\rm eff}(\lambda_{\rm rest}, z_q)$ – the effective optical depth as a function of rest wavelength, $\lambda_{\rm rest}$, for quasars with redshift z_q. The shape of this curve depends on $\lambda_{\rm eff}$, and Prochaska, Worseck & O'Meara (2009) stacked QSO spectra in bins of z_q to measure $\lambda_{\rm eff}(z)$. They argued that this method has the advantage that it determines $\lambda_{\rm eff}$ without the need to measure the CDDF in the regime of LLS's where it is especially hard to determine the column density of these saturated lines. Here, we will show that the actual shape of $\tau_{\rm eff}$ also depends on the CDDF, so inferring $\lambda_{\rm eff}$ still requires making assumptions on the shape of the CDDF in the regime of LLS's.

Prochaska, Worseck & O'Meara (2009) model $\tau_{\rm eff}(\lambda_{\rm rest}, z_q)$ as[16]

$$\tau_{\rm eff}(\lambda_{\rm rest}, z_q) = \frac{2}{9} \frac{(1+z_q)^{3/2}}{X_{\rm eff}(z_q)\Omega_m^{1/2}} \left(\frac{\lambda_{\rm rest}}{\lambda_{\rm th}} \right)^{-3/2} \left[1 - \left(\frac{\lambda_{\rm rest}}{\lambda_{\rm th}} \right)^{9/2} \right]. \tag{27}$$

---

[15] Absorption may also be due to other lines of hydrogen or indeed lines from other elements. We will ignore these in this section.

[16] This is equation (6) of Prochaska, Worseck & O'Meara (2009), setting their redshift-dependent opacity $\tilde{\kappa}_{912}(z') \to \tilde{\kappa}_{912}(z_q) = \lambda_{\rm eff}^{-1}(z_q)$, the proper attenuation length at redshift z_q, and then converting $\lambda_{\rm eff}(z_q) \to X_{\rm eff}$.

Here, $\lambda_{\rm rest}$ is the wavelength *in the rest frame of the quasar*, *i.e.* the observed wavelength is $\lambda_{\rm rest}(1 + z_q)$. To derive this expression, Prochaska, Worseck & O'Meara (2009) assume that the effective opacity is of the form

$$\kappa_{912}(z', z_q, \lambda_{\rm rest}) \equiv \frac{{\rm d}\tau_{\rm eff}(z', \lambda_{\rm rest})}{{\rm d}l} \approx \tilde{\kappa}_{912}(z_q) \left[\frac{\lambda_{\rm rest}(1 + z')}{\lambda_{\rm th}(1 + z_q)} \right]^3, \quad (28)$$

where they argue that the wavelength dependence is approximate, and further assume that $\tilde{\kappa}_{912}(z')$ is approximately constant over the small wavelength range studied, so that it can be evaluated at $z' \to z_q$. The attenuation length at the mean redshift of the sample of QSO's is determined by fitting the data to this model. For wavelengths close to $\lambda_{\rm th}$ we find

$$\tau_{\rm eff}(\lambda_{\rm rest} \lesssim \lambda_{\rm th}, z_q) \approx \frac{(1 + z_q)^{3/2}}{X_{\rm eff}(z_q)\Omega_m^{1/2}} \left(1 - \frac{\lambda_{\rm rest}}{\lambda_{\rm th}} \right). \quad (29)$$

Our own, slightly different, derivation goes as follows. The effective optical depth measured by an observer at redshift z_o at wavelength λ_o in a stack of QSO spectra with emission redshift z_q, is

$$\tau_{\rm eff}(\lambda_o, z_o, z_q) = \int_{z_S}^{z_q} {\rm d}z'[1 + b_S\, b_{\rm LLS}\xi(z', z_q)]$$
$$\times \int_0^\infty {\rm d}N_{\rm H{\small I}} \frac{{\rm d}X}{{\rm d}z'} f(N_{\rm H{\small I}}, z') \left[1 - \exp(-\tau) \right], \quad (30)$$

for $\lambda_o \le \lambda_{\rm th}(1 + z_q)/(1 + z_o)$ and zero otherwise. To see why, notice that the inner integral sums the contribution to $\tau_{\rm eff}$ over column density whereas the outer integral sums over all intervening absorbers that cause bound-free absorption at wavelength λ_o. For wavelengths close to $\lambda_{\rm th}$ in the rest frame of the quasar, only absorbers with redshift close to z_q contribute to the integral over z, because the photon's wavelength will be redshifted below the Lyman limit when z is too low. For wavelengths shorter than $\lambda_{\rm th}$ in the rest frame of the observer, all absorbers with $z_o \lesssim z \lesssim z_q$ contribute to the absorption. The lower limit to the integral over z' is therefore

$$z_S = \max\left[z_o, \frac{\lambda_o}{\lambda_{\rm th}}(1 + z_o) - 1 \right]. \quad (31)$$

The quantity τ in equation (30) is the optical depth (and not the effective optical depth) measured by the observer (at redshift z_o) at wavelength λ_o due to an absorber with column density $N_{\rm H{\small I}}$ at redshift z' (with $z_o \le z' \le z_q$), $\tau = \sigma \times N_{\rm H{\small I}}$. The photoionization cross section, σ, is a function of the ratio of the Lyman-limit wavelength $\lambda_{\rm th} \approx 912.1$ Å, over the wavelength of the photon in the rest frame of the absorber. The latter wavelength is $\lambda_o \times (1 + z_o)/(1 + z')$. We will write the wavelength dependence of σ as (e.g. Verner et al. 1996)

$$\sigma(\lambda) = \sigma_{\rm th} \times \left(\frac{\lambda_{\rm th}}{\lambda} \right)^{-3} \equiv \sigma_{\rm th} \times s\left(\frac{\lambda_{\rm th}}{\lambda}\right), \quad (32)$$

with the function s encoding the wavelength dependence. Substituting this in the expression for τ then yields

$$\tau(\lambda_o, z_o, N_{\rm H{\small I}}, z') = \sigma_{\rm th} \times N_{\rm H{\small I}} \times s\left(\frac{\lambda_{\rm th}(1 + z')}{\lambda_o(1 + z_o)} \right). \quad (33)$$

We now change the integration variable in the inner integral of equation (30) from $N_{\rm H{\small I}} \to \tau$, using equation (33). This allows us to write equation (30) in terms of $X_{\rm eff}$ evaluated at $\lambda_{\rm th}$ and redshift z' as

$$\tau_{\rm eff}(\lambda_o, z_o, z_q) = \int_{z_S}^{z_q} {\rm d}z' \frac{{\rm d}X/{\rm d}z'}{X_{\rm eff}(z')} \left[1 + b_S\, b_{\rm LLS}\xi(z', z_q) \right]$$
$$\times \left[s\left(\frac{\lambda_{\rm th}(1 + z')}{\lambda_o(1 + z_o)} \right) \right]^{2/3}. \quad (34)$$

We can compare this (more general) expression to the special case considered by Prochaska, Worseck & O'Meara (2009) by setting $z_o = 0$ and $\lambda = \lambda_o$ (since we are the observer), and making the same four approximations that resulted in equation (29): (i) replace $X_{\rm eff}(z') \to X_{\rm eff}(z_q)$ (i.e. assume that the absorption distance does not change appreciably over the small redshift interval), (ii) take the cross-section $s(x) = x^3$, (iii) neglect clustering of absorbers (*i.e.* take $b_S \times b_{\rm LLS} = 0$), and finally (iv) obtain an expression for sufficiently long wavelengths so that we can take $z_S = z_o$. This yields

$$\tau_{\rm eff}(\lambda = \lambda_o, z_o = 0, z_q) \approx \frac{2}{X_{\rm eff}(z_q)\Omega_m^{1/2}} \left(\frac{\lambda}{\lambda_{\rm th}} \right)^{3/2}$$
$$\times \left\{ 1 - \left[\frac{\lambda}{\lambda_{\rm th}(1 + z_q)} \right]^{1/2} \right\}, \quad (35)$$

The limit of this expression for $\lambda \to \lambda_{\rm th}(1 + z_q)$ is identical to equation (29), that is, our alternative expression equation (34) is identical to that of Prochaska, Worseck & O'Meara (2009) close to the quasar (when neglecting bias). However, they differ further away from the QSO. The reason for the difference becomes clear when looking at equation (3) of Prochaska, Worseck & O'Meara (2009), where it is assumed that the 'opacity' $\kappa \propto f(N_{\rm H{\small I}}) \exp(-\tau) \propto \lambda^3$, whereas in our case the scaling is $\propto s^{2/3} \propto \lambda^2$ in the case of $s(x) \propto x^3$. We note that (i) the dependence on wavelength depends on the *slope* of the assumed CDDF (which is 5/3 in our model), and (ii) the scaling $s(x) \propto x^3$ is only approximately valid, and it would be better to use a more accurate expression for the photoionization cross section (e.g. Verner et al. 1996). A final difference in our derivation compared to that of Prochaska, Worseck & O'Meara (2009) is that we assume that $X_{\rm eff}$ is approximately constant, which is not the same as assuming that $\tilde{\kappa}_{912}(z') \propto (1 + z')^3/X_{\rm eff}(z')$ is constant over the relevant redshift interval (*i.e.* opacity is not a co-moving quantity).

To test our expression, we generate mock absorption spectra as follows. Choosing a value for z_q and assuming that the CDDF is of the form $f(N_{\rm H{\small I}}) = f_0 \times (10^{17.2}\, {\rm cm}^{-2}/N_{\rm H{\small I}})^{5/3}$ for some amplitude f_0, we generate the optical depth as a function of wavelength of the form

$$\tau(\lambda, z_q) = \sum_{z=z_{912}}^{z_q} \sum_{N_{\rm H{\small I}}=0}^\infty N(N_{\rm H{\small I}}, z)\tau(\lambda, N_{\rm H{\small I}}, z), \quad (36)$$

where τ is the optical depth at wavelength λ due to an absorber with column density $N_{\rm H{\small I}}$ at redshift z, taken from equation (33), and $N(N_{\rm H{\small I}}, z)$ is the Poisson distributed number of lines with CDDF $f(N_{\rm H{\small I}})$. The mean of this Poisson distribution is $({\rm d}X/{\rm d}z)\, f(N_{\rm H{\small I}})\, \Delta N_{\rm H{\small I}}\, \Delta z$, where $\Delta N_{\rm H{\small I}}$ and Δz are the steps in the sums over column density and redshift in equation (36). For a given realisation of $\tau(\lambda, z)$, we can compute the transmission, $\exp(-\tau)$, and averaging over many realization the effective optical depth, $\langle \exp(-\tau) \rangle \equiv \exp(-\tau_{\rm eff})$. The results of this exercise are summarized in Fig. 7, which shows that within our assumed approximations, equation (35) (solid red line) reproduces $\tau_{\rm eff}(\lambda_{\rm rest})$ from the simulation very well, with equation (35) (dashed yellow line) capturing correctly the gradient of this curve close to $\lambda_{\rm th}$. The original expression equation (29) from Prochaska, Worseck & O'Meara (2009) (yellow dotted line) falls a little below the simulated results (blue line).

Finally, we note that biasing and the QSO's proximity effect (*i.e.* the fact that the QSO itself emits ionising radiation) will likely play an increasingly important role at higher z. We could account for the proximity effect by replacing $\Gamma \to \Gamma_0 + \Gamma_q(z)$ in the expression for $X_{\rm eff}$ of equation (5), where $\Gamma_q(z)$ is the photoionization rate at redshift z due to the QSO itself.
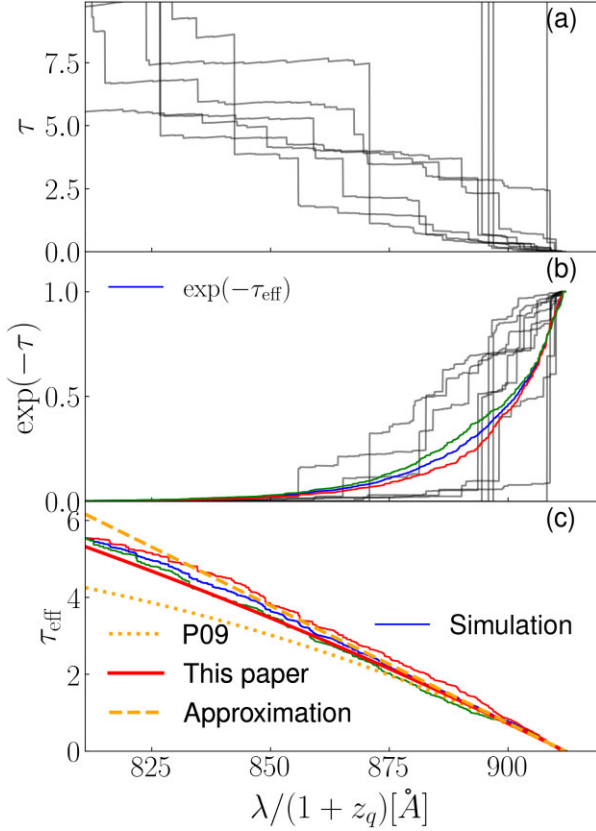
Figure 7. Mock spectra and effective optical depths as a function of rest-wavelength, $\lambda_{rest} \equiv \lambda/(1 + z_q)$. *Top panel:* Lyman-limit optical depth for 10 mock spectra generated using Poisson-distributed absorption lines. *Central panel:* corresponding transmission $\exp(-\tau)$ for these spectra (*black thin lines*) and mean transmission for 200 realizations (*blue solid line*). The wavy nature of $\exp(-\tau_{eff})$ reflects the relatively large spectrum-to-spectrum variations, a consequence of the relatively low number density of strong absorbers that dominate the optical depth. *Lower panel:* effective optical depth for the simulated spectra (*blue thin solid line*), the approximation from Prochaska, Worseck & O'Meara (2009) (*yellow dotted line* labelled 'P09'), equation (30), and the approximation in this paper (*red line*), equation (34) with $b_S = 0$. *Red* and *green thin solid lines* in panels (a) and (b) show the simulation estimates using 100 (rather than 200) realizations. Numerically, we set $z_q = 6$, $X_{eff} = 0.607$ is kept constant, integrated the CDDF from $\log N_{\rm H\,I}[cm^{-2}] = 14 \rightarrow 22$ in steps of 0.025 dex, and used integration steps of 0.05 Å in λ_{rest}.

4.1 The transition to a transparent Universe

To interpret the general expression for τ_{eff} of equation (34) qualitatively, it is useful to make the following approximations, (i) use the high-z expression for the Hubble constant, (ii) assume that the hydrogen photoionization cross section has wavelength dependence $\sigma \propto \lambda^3$, (iii) take the absorption distance $X_{eff}(z')$ in the expression to be constant at its value for $z = z_q$, and (iv) neglect clustering ($b_S \times b_{LLS} \rightarrow 0$). This yields the following analytical expressions

$$\tau_{eff}(\lambda_{rest}, z_o, z_q) \approx \frac{2}{X_{eff}(z_q)\Omega_m^{1/2}} \left[\frac{\lambda_{rest}(1+z_q)}{\lambda_{th}} \right]^{3/2}$$
$$\times \left[1 - \left(\frac{\lambda_{rest}}{\lambda_{th}} \right)^{1/2} \right], \tag{37}$$
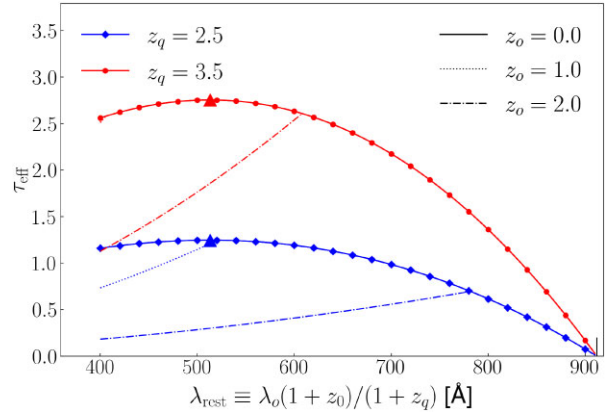
Figure 8. Effective optical depth, τ_{eff}, as a function of wavelength, λ_{rest}, measured in the rest-frame of the QSO, as given by equations (37) and (38). The *red line connecting filled circles* and the *blue line connecting filled diamonds* correspond to QSO redshifts of $z_q = 2.5$ and 3.5, the observer's redshifts are 0, 1, and 2 for *solid, dotted, and dotted–dashed lines*. The location and value where τ_{eff} reaches a maximum, given by equation (39) are indicated by a large filled triangle. The Lyman limit rest wavelength is indicated by a small vertical line.

for $\lambda_{th}(1 + z_o)/(1 + z_q) \le \lambda_{rest} \le \lambda_{th}$, and

$$\tau_{eff}(\lambda_{rest}, z_o, z_q) \approx \frac{2}{X_{eff}(z_q)\Omega_m^{1/2}} \left[\frac{\lambda_{rest}(1+z_q)}{\lambda_{th}} \right]^2$$
$$\times \frac{1}{(1+z_o)^{1/2}} \left[1 - \left(\frac{1+z_o}{1+z_q} \right)^{1/2} \right], \tag{38}$$

for $\lambda_{rest} \le \lambda_{th}(1 + z_o)/(1 + z_q)$, where as before, λ_{rest} is the photon's wavelength in the rest frame of the QSO. The first expression has a maximum optical depth, $\tau_{eff,max}$ which occurs at a rest-wavelength λ_{max}, given by

$$\lambda_{rest,max} = \left(\frac{3}{4} \right)^2 \lambda_{th}$$

$$\tau_{eff,max} \approx 0.105 \times \frac{2}{X_{eff}(z_q)\Omega_m^{1/2}} (1+z_q)^{3/2}. \tag{39}$$

The motivation for computing these expressions for observers at different redshifts – and not just for $z_o = 0$ – is that $\tau_{eff}(\lambda_{rest}, z_o, z_q)$ can be used to compute the photoionization rate at redshift z_o due to a QSO at higher z.

The resulting run of optical depth with wavelength is plotted in Fig. 8 for two QSO redshifts ($z_q = 2.5$ and 3.5) and three observer redshifts ($z_o = 0$, 1 and 2). The shape of these curves can be understood as follows. Photons with rest wavelength close to λ_{th} can only be absorbed by absorbers close to the QSO before they redshift below the Lyman limit of intervening neutral gas. Therefore the redshift path where an absorber affects the photon lengthens with decreasing λ_{rest}: this is why τ_{eff} initially increases with decreasing wavelength. There are two reasons why τ_{eff} eventually starts to decrease again with decreasing λ_{rest}. First, once a photon's wavelength becomes smaller than λ_{th} in the rest frame of the observer, $z_S \rightarrow z_o$, the redshift range that contains absorbers, ceases to lengthen. The optical depth then drops because the photoionization cross section drops, and τ_{eff} is given by equation (38) rather than equation (37). This sudden change is illustrated by the dotted and dotted–dashed lines that branch away from the solid line in the Figure. Secondly, τ_{eff} starts to decrease once $\lambda_{rest} \le (3/4)^2\lambda_{th}$, even when τ_{eff} is described by equation (37). This occurs because the tension between τ_{eff} increasing due to the
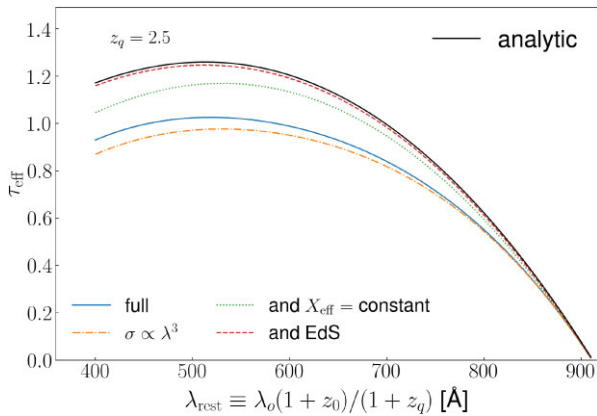
Figure 9. Same as Fig. 8 but for a QSO at $z_q = 2.5$ and an observer at $z_o = 0$. The *solid blue line* is obtained by numerically integrating equation (34). The other line styles are successive approximations: the *dotted–dashed orange line* takes the photoionization cross-section to be $\propto \lambda^{-3}$ rather than the more accurate expression from Verner et al. (1996), the *dotted green line* in addition takes $X_{\mathrm{eff}}(z)$ constant at its value at $z = z_q$, and the *dashed red line* in addition assumes an EdS universe, $H(z) = H_0\,\Omega_m^{1/2}(1+z)^{3/2}$. The *solid black line* is the analytical expression from equations (37) and (38) which makes the same approximations as the *dashed red line*; it has been off-set vertically by a factor 1.01 to avoid complete overlap with that line.

increasing redshift path (due to the factor $1 - (\lambda_{\mathrm{rest}}/\lambda_{\mathrm{th}})^{1/2}$) and τ_{eff} decreasing due to the decreasing photoionization cross-section (the factor $(\lambda_{\mathrm{rest}}/\lambda_{\mathrm{th}})^{3/2}$) is eventually decided in favour of the latter process. We note that the decrease in τ_{eff}, in this case, is *not* due to the decrease in the co-moving number of absorbers at lower redshifts, since in the approximation that leads to these equations we have kept X_{eff} constant.

Although equations (37)–(38) are useful for describing the qualitative behaviour of τ_{eff}, they are not particularly accurate because the approximations made in deriving them from equation (34) are not very accurate, as we illustrate in Fig. 9. Of the various approximations made, we see that accounting for the evolution of X_{eff} has the largest impact. Indeed, if we allow X_{eff} to increase with decreasing z using equation (15), the value of $\tau_{\max}$ is reduced by about 20 per cent for this particular choice of z_q.

Finally, we note that τ_{eff} reaches a maximum value of $\sim$1 for a QSO at redshift $z_q \sim 2.5$. This means that below a redshift of 2.5, most QSO's contribute to ionizing neutral hydrogen atoms at all lower z, *i.e.* the Universe becomes 'transparent' to ionizing radiation. Indeed, unless the atoms are in a self-shielded region, intervening absorbers typically decrease the ionizing flux by less than a factor of $1/e$. Madau, Haardt & Rees (1999) referred to this epoch as 'breakthrough'. Their value of the breakthrough redshift of $\sim$1.6 is lower than our value of 2.5. The reason is that they assumed that $X_{\mathrm{eff}} \propto (1+z)^{-3/2}$ with a normalization set by the CDDF at $z = 3$; they also use a different slope for the CDDF.

5 SUMMARY AND CONCLUSIONS

We presented an analytical model for the CDDF of hydrogen absorption lines along a sight line piercing the intergalactic medium (IGM; equation 14). The model assumes that cosmic gas in dark matter haloes follows a power-law distribution in density, $\rho(R) \propto R^{-2}$, and is photoionized by an evolving radiation background with amplitude $\Gamma_0(z) \equiv \Gamma_{-12} \times 10^{-12}\,\mathrm{s}^{-1}$, as computed by Haardt & Madau (2012). The resulting CDDF reproduces well the observed CDDF at redshift z

~ 3 for hydrogen column densities $\log N_{\mathrm{H\,I}}[\mathrm{cm}^{-2}]$ in the range [14 $\to$ 16], and [20 $\to$ 22], where the CDDF is well-measured (Fig. 1). The analytical expression for the CDDF contains one free parameter, f_{gas}, which is of order unity, and some extra parameters such as the temperature of the gas for which we use observed values. The evolution of the model's CDDF is due to (i) the evolution of $\Gamma_{-12}(z)$, (ii) the evolution of M_{crit}, which is the halo mass below which haloes lose their gas due to photoheating by the radiation background, (iii) the dependence of the virial temperature of a halo of given mass on z, and finally, and to a lesser extent, (iv) the evolution of the halo mass function. Our model builds on that of Theuns (2021), as well as earlier models by Miralda-Escudé, Haehnelt & Rees (2000) and Muñoz et al. (2016).

We then use the model to compute the evolution of the attenuation length of ionizing photons, λ_{eff} (see equation 16). The evolution of λ_{eff} is dominated by cosmological expansion, while the co-moving evolution is due to the evolution of the CDDF. We find that the model's evolution of λ_{eff} agrees very well with the observed evolution in the redshift range $z = 2 \to 5$, but not for $z > 5$ where the data evolve much faster than the model (Fig. 1). Even though the model reproduces the value of λ_{eff} at $z \sim 3$ very well, it underestimates the number of absorption lines with $\log N_{\mathrm{H\,I}}(\mathrm{cm}^{-2}) > 17.5$ by about a factor of 2 (see Fig. B1).

Since absorption lines occur when a sight line intersects a halo in our model, we can relate the clustering of haloes to that of the corresponding absorbers. The bias of Lyman-limit systems (LLS's) is $\sim$1.5 at $z = 2$, increasing to $b \sim 2.6$ at $z = 6$ (Fig. 4). At first surprising, we find that the bias of damped Lyman α systems (DLA's) with $\log N_{\mathrm{H\,I}}(\mathrm{cm}^{-2}) = 20.3$ is *lower* than that of LLS. The reason is that self-shielding – which causes the transition from highly ionized LLS's to mostly neutral DLA's – sets in at lower column density in lower mass haloes – and such haloes are less biased. At even higher columns, the bias of DLA's increases rapidly with increasing $N_{\mathrm{H\,I}}$.

We account for clustering between absorbers and quasars, assuming that quasars inhabit dark matter haloes with masses $M_{\mathrm{h}} \approx 10^{12-13}$ $\mathrm{M}_\odot$ (Fig. 5), and reach the following conclusions. Bias has little effect on the value of λ_{eff} inferred from quasar spectra below $z \sim 4$. However, the rapid increase in quasar host bias above this redshift leads to a corresponding rapid decrease in the value of λ_{eff} inferred from analysing quasar spectra, and this brings the model's evolution of λ_{eff} into line with the observations, also at $z \sim 6$. It is important to realize that this finding has potential implications when studying the tail-end of reionization at $z \sim 6$: the value of λ_{eff} *measured in quasar spectra* is generally less (by almost an order of magnitude) than the value of λ_{eff} in the IGM. This makes it harder for quasars to ionize the IGM, since they are surrounded by many more absorbers than galaxies: $\Gamma \propto \lambda_{\mathrm{eff}}$ so that galaxies contribute more to the ionizing background than quasars, *even in the case that both population had the same emissivity.*[17] We use our model to calculate the statistics of the attenuation length for rays of a given length in Section 3.3 (see Fig. 6). We find that the distribution of mean transmissions for rays with a given length of the order of λ_{eff} has a long tail to very large values of τ_{eff}, a consequence of the fact that the absorption is dominated by relatively strong absorbers which are rare.

In the final section, Section 4, we use the model to compute the mean transmission, $T(\lambda_{\mathrm{rest}}, z_q)$, due to Lyman-limit absorption (where

---

[17]Note that the bias we compute is the two-halo term: the absorbers we consider inhabit a different halo from the source. There may be an additional effect from associated absorbers. We also note that we have not accounted for other proximity effects.

$\lambda_{\rm rest}$ is wavelength in the QSO's rest frame and z_q the redshift of the quasar in which T is measured). We relate T to the amplitude and slope of the CDDF around column densities $\sim 10^{17.2}$ cm^{-2}, and examine how it is affected by various commonly made simplifications. Our general expression, equation (34), reduces to that derived by Prochaska, Worseck & O'Meara (2009) for wavelengths close to 912 Å in the rest frame of the quasar, but differs at shorter wavelengths. We find that the minimum transmission T stays above e^{-1} (i.e. the corresponding effective optical depth remains below 1) on average when $z_q \lesssim 2.5$, which is, therefore, the earliest redshift below which the Universe becomes transparent to ionizing photons.

This paper shows that a simple model for gas in haloes accurately predicts the evolution of the CDDF and that of the associated attenuation length. The model also allows us to account for bias and clustering. Of course, our analytical model is not as accurate nor as realistic as numerical simulations, but it illustrates well the dominant properties of haloes and the IGM that give rise to the observables. Several aspects of the model could be further improved. These include accounting for scatter in the gas properties for haloes of a given mass and deviations from spherical symmetry, and a more accurate treatment of the temperature of the absorbing gas. The model assumes that the density profile of the gas[18] is $\rho(R) \propto R^{-2}$, and it would be worthwhile examining why this assumption works so well. In the model, the majority of strong absorbers occur in the outskirts of dark matter haloes, with some smaller fractions occurring outside the virial radius of the halo. This is consistent with the observation that such absorbers also correlate strongly with the presence of nearby galaxies (Lofthouse et al. 2023). This also implies that the sources of the ionizing photons inhabit the same dark matter haloes as the sinks. It would be worth exploring whether this correlation can be accounted for (see e.g. Muñoz et al. 2016), rather than combining a model for the absorbers with the Haardt & Madau (2012) model for the ionizing background as we did here.

ACKNOWLEDGEMENTS

[18]It would be easy to redo the calculations for another assumed power-law.

DATA AVAILABILITY

This paper does not contain any new data.

REFERENCES

Alonso D., Colosimo J., Font-Ribera A., Slosar A., 2018, J. Cosmol. Astropart. Phys., 2018, 053
Altay G., Theuns T., Schaye J., Crighton N. H. M., Dalla Vecchia C., 2011, ApJ, 737, L37
Altay G., Theuns T., Schaye J., Booth C. M., Dalla Vecchia C., 2013, MNRAS, 436, 2689
Bahcall J. N., Peebles P. J. E., 1969, ApJ, 156, L7
Becker G. D., D'Aloisio A., Christenson H. M., Zhu Y., Worseck G., Bolton J. S., 2021, MNRAS, 508, 1853
Bohm G., Zech G., 2014, Nucl. Instrum. Methods Phys. Res. A, 748, 1
Bosman S. E. I. et al., 2022, MNRAS, 514, 55
Bower R. G., Schaye J., Frenk C. S., Theuns T., Schaller M., Crain R. A., McAlpine S., 2017, MNRAS, 465, 32
Cain C., D'Aloisio A., Gangolli N., Becker G. D., 2021, ApJ, 917, L37
Cain C., D'Aloisio A., Iršič V., Gangolli N., Dhami S., 2023, J. Cosmol. Astropart. Phys., 2023, 002
Crighton N. H. M., Prochaska J. X., Murphy M. T., O'Meara J. M., Worseck G., Smith B. D., 2019, MNRAS, 482, 1456
D'Aloisio A., McQuinn M., Trac H., Cain C., Mesinger A., 2020, ApJ, 898, 149
Davies F. B. et al., 2018, ApJ, 864, 142
de Beer S. et al., 2023, MNRAS, 526, 1850
Diemer B., 2018, ApJS, 239, 35
Erkal D., 2015, MNRAS, 451, 904
Fan X. et al., 2006, AJ, 132, 117
Faucher-Giguère C.-A., Kereš D., 2011, MNRAS, 412, L118
Faucher-Giguère C.-A., Lidz A., Zaldarriaga M., Hernquist L., 2009, ApJ, 703, 1416
Fumagalli M., Prochaska J. X., Kasen D., Dekel A., Ceverino D., Primack J. R., 2011, MNRAS, 418, 1796
Fumagalli M., O'Meara J. M., Prochaska J. X., Worseck G., 2013, ApJ, 775, 78
Gaikwad P. et al., 2023, MNRAS, 525, 4093
Garaldi E., Kannan R., Smith A., Springel V., Pakmor R., Vogelsberger M., Hernquist L., 2022, MNRAS, 512, 4909
Gunn J. E., Peterson B. A., 1965, ApJ, 142, 1633
Haardt F., Madau P., 1996, ApJ, 461, 20
Haardt F., Madau P., 2012, ApJ, 746, 125
Hunter J. D., 2007, Comput. Sci. Engi., 9, 90
Jones E., Oliphant T., Peterson P. et al., 2001, SciPy: Open Source Scientific Tools for Python, http://www.scipy.org/
Keating L. C., Weinberger L. H., Kulkarni G., Haehnelt M. G., Chardin J., Aubert D., 2020, MNRAS, 491, 1736
Kim T. S. et al., 2021, MNRAS, 501, 5811
Lofthouse E. K. et al., 2023, MNRAS, 518, 305
Lusso E., Fumagalli M., Rafelski M., Neeleman M., Prochaska J. X., Hennawi J. F., O'Meara J. M., Theuns T., 2018, ApJ, 860, 41
Madau P., Haardt F., Rees M. J., 1999, ApJ, 514, 648
Mason C. A., Treu T., Dijkstra M., Mesinger A., Trenti M., Pentericci L., de Barros S., Vanzella E., 2018, ApJ, 856, 2
McQuinn M., 2016, ARA&A, 54, 313
McQuinn M., Oh S. P., Faucher-Giguère C.-A., 2011, ApJ, 743, 82
Meiksin A. A., 2009, Rev. Mod. Phys., 81, 1405
Meiksin A., Madau P., 1993, ApJ, 412, 34
Miralda-Escudé J., 2003, ApJ, 597, 66
Miralda-Escudé J., Haehnelt M., Rees M. J., 2000, ApJ, 530, 1
Mo H., van den Bosch F. C., White S., 2010, Galaxy Formation and Evolution. Cambridge Univ. Press, Cambridge
Mortlock D. J. et al., 2011, Nature, 474, 616
Muñoz J. A., Oh S. P., Davies F. B., Furlanetto S. R., 2016, MNRAS, 455, 1385
Noterdaeme P. et al., 2012, A&A, 547, L1

O'Meara J. M., Prochaska J. X., Worseck G., Chen H.-W., Madau P., 2013, ApJ, 765, 137

Okamoto T., Gao L., Theuns T., 2008, MNRAS, 390, 920

Onoue M. et al., 2017, ApJ, 847, L15

Paresce F., McKee C. F., Bowyer S., 1980, ApJ, 240, 387

Pérez-Ràfols I., Miralda-Escudé J., Arinyo-i-Prats A., Font-Ribera A., Mas-Ribas L., 2018, MNRAS, 480, 4702

Pérez-Ràfols I., Pieri M. M., Blomqvist M., Morrison S., Som D., Cuceu A., 2023, MNRAS, 524, 1464

Planck Collaboration XIII, 2016, A&A, 594, A13

Planck Collaboration VI, 2020, A&A, 641, A6

Press W. H., Schechter P., 1974, ApJ, 187, 425

Prochaska J. X., Worseck G., O'Meara J. M., 2009, ApJ, 705, L113

Prochaska J. X., O'Meara J. M., Worseck G., 2010, ApJ, 718, 392

Rahmati A., Pawlik A. H., Raičević M., Schaye J., 2013, MNRAS, 430, 2427

Rauch M., 1998, ARA&A, 36, 267

Reed D. S., Bower R., Frenk C. S., Jenkins A., Theuns T., 2007, MNRAS, 374, 2

Ribaudo J., Lehner N., Howk J. C., 2011, ApJ, 736, 42

Rudie G. C., Steidel C. C., Shapley A. E., Pettini M., 2013, ApJ, 769, 146

Schaye J., Theuns T., Rauch M., Efstathiou G., Sargent W. L. W., 2000, MNRAS, 318, 817

Theuns T., 2021, MNRAS, 500, 2741

Verner D. A., Ferland G. J., Korista K. T., Yakovlev D. G., 1996, ApJ, 465, 487

van der Walt S., Colbert S. C., Varoquaux G., 2011, Comput. Sci. Engi., 13, 22

Worseck G. et al., 2014, MNRAS, 445, 1745

Yajima H., Choi J.-H., Nagamine K., 2012, MNRAS, 427, 2889

Zhang H., Behroozi P., Volonteri M., Silk J., Fan X., Hopkins P. F., Yang J., Aird J., 2023, MNRAS, 518, 2123

Zheng Z., Miralda-Escudé J., 2002a, ApJ, 568, L71

Zheng Z., Miralda-Escudé J., 2002b, ApJ, 578, 33

van de Voort F., Schaye J., Altay G., Theuns T., 2012, MNRAS, 421, 2809

APPENDIX A: ATTENUATION LENGTH VERSUS MEAN FREE PATH

We relate the mean free path to the attenuation length due to a distribution of absorbers as follows. Consider a Poisson distribution of absorbers with mean number density per unit distance μ, all of which have the same optical depth, τ_i. The probability of having more than N' such absorbers in a distance L, is given by

$$\mathcal{P}(> N'|L) = 1 - \mathcal{P}(N = 0, 1, 2, \cdots N'|L) = 1 - \sum_{N=0}^{N'} \mathbb{P}(N'|N\mu L),$$
(A1)

where $\mathbb{P}(x|y) \equiv y^x \exp(-y)/x!$ is the Poisson distribution. The probability of reaching N' absorbers after travelling a distance between L and $L + dL$ is the derivative of this cumulative distribution with respect to L, which is the Gamma distribution

$$\mathcal{P}(L) = \frac{\mu \exp(-\mu L) (\mu L)^{N'-1}}{(N' - 1)!}.$$
(A2)

This is a well-known result in statistics.

We define the free path of a photon to be the distance it travelled before encountering an optical depth $\tau > 1$. In our case, this corresponds to encountering more than $N' = 1/\tau_i$ absorbers. The PDF of the free path is therefore given by equation (A2), provided we set $N' = 1/\tau_i$. The mean value of the free path – *i.e.* the mean free path – is then

$$\lambda = \langle L \rangle = \int_0^\infty \mathcal{P}(L)\, dL = \frac{(\tau_i^{-1} + 1)\, \Gamma(\tau_i^{-1})}{\mu\, (\tau_i^{-1} - 1)!} \approx \frac{1}{\tau_i \mu}.$$
(A3)

On the other hand, the effective optical depth encountered after travelling a distance L, is

$$\tau_{\text{eff}}(L) = \mu\, L\, (1 - \exp(-\tau_i)).$$
(A4)

The attenuation length, λ_{eff} – the distance travelled to reach $\tau_{\text{eff}} = 1$ – is therefore

$$\lambda_{\text{eff}} = \frac{1}{\mu\, (1 - \exp(-\tau_i))}.$$
(A5)

Comparing equation (A3) to equation (A5) shows that the attenuation length equals the mean free path in the limit of $\tau_i \ll 1$, but for $\tau_i = 0.5$, for example, $\lambda = 2/\mu$ but $\lambda_{\text{eff}} = 2.5/\mu$.

Consider now the case of $\tau_i \to \infty$. In that limit, the free path is the distance travelled up to the first absorber, therefore the PDF of L becomes

$$\mathcal{P}(L) = \frac{1}{\mu} \mathbb{P}(0|\mu L) = \frac{1}{\mu} \exp(-\mu\, L),$$
(A6)

so that the mean free path is $\lambda = \langle L \rangle = \mu^{-1}$. The mean transmission after a distance L is the fraction of paths that did not encounter an absorber, $\exp(-\tau_{\text{eff}}(L)) = \mathbb{P}(0|\mu L)$. Therefore, the attenuation length is $\lambda_{\text{eff}} = \mu^{-1}$ – and hence equals the mean free path.

In conclusion: when absorption is dominated by very strong absorbers (the case of $\tau_i \to \infty$) or in the case of a uniform IGM (the case of $\tau_i \to 0$), mean free path and attenuation length have the same numerical value. However, if a significant fraction of the absorption is due to absorbers with optical depth of order unity, then the attenuation length is larger than the mean free path. The latter case applies to Lyman-limit absorption in the IGM. The attenuation length is often and erroneously referred to as mean free path in the literature – which is unfortunate.

APPENDIX B: THE EVOLUTION OF THE NUMBER DENSITY OF LLS

Crighton et al. (2019) review different methods for identifying strong H I absorbers in QSO spectra. They then present results of a survey for such absorbers in a homogeneous data set of 153 QSO spectra at redshift $z \sim 5$ from the Giant Gemini GMOS survey (Worseck et al. 2014). Combining values from the literature with their own analysis, they present the evolution of the number density of strong absorbers in terms of the co-moving quantity $l(X)$, which is the mean number density of absorbers (with column density larger than some value) per unit co-moving path length, X. They count absorbers with $N_{\text{H I}} > 10^{17.5}$ cm^{-2} because these can be identified confidently given the limited signal-to-noise ratio of their data.

Given that $l(X)$ is a number density of absorbers, we prefer to use the notation dN/dX, rather than $l(X)$, since $l(X)$ is easily mistaken for a length. Without further ado, we find the following relation between $dN/dX \equiv l(X)$ and the CDDF, where on the second line we substitute the approximate relation of equation (13) for the CDDF,

$$\frac{dN}{dX}(z) = \int_{10^{17.5}\text{cm}^{-2}}^\infty f(N_{\text{H I}})\, dN_{\text{H I}} \approx 0.2\, \frac{f_{17.2}(z)}{\Gamma_{-12}^{2/3}(z)}.$$
(B1)

This relation follows from either integrating the CDDF of equation (12) from $N_{\text{H I}} = 10^{17.5}$ cm$^{-2} \to \infty$ or directly from equation (10). The latter route makes it clearer why dN/dX does not depend on the shape of the CDDF for $N_{\text{H I}} > 10^{17.5}$ cm^{-2}.

Fig. B1 compares the evolution predicted by the model to the observations plotted in fig. 9 of Crighton et al. (2019). The data are compiled from Prochaska, O'Meara & Worseck (2010), Ribaudo, Lehner & Howk (2011), O'Meara et al. (2013), and Fumagalli
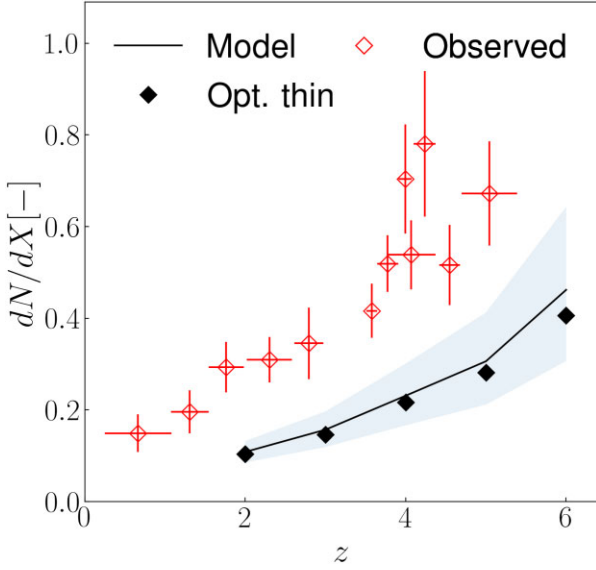
Figure B1. Evolution of the mean number density of absorbers with optical depth $\tau > 2$. The *black solid line* is the evolution predicted by the model of TT21, the *grey shading* corresponds to varying the value of the parameter M_{crit} by factors between 1/4 and 4. The *black solid diamonds* are the approximate evolution of the model from equation (B1) using the power law of the CDDF from equation (12). *Red symbols with error bars* are the observed data plotted in fig. 9 of Crighton et al. (2019). Model and cosmological parameters are as in Fig. 1.

et al. (2013), in addition to data from Crighton et al. (2019). We first note that the optically thin approximation (black diamonds) reproduces almost exactly TT21's model that includes self-shielding (black curve). Both underestimate the observed number density (red diamonds) by a factor ~ 2 yet reproduce the observed evolution very well. It is somewhat surprising that the model described so far reproduces λ_{eff} well for $z \leq 5$ as seen in Fig. 1 (right-hand panel) yet it underestimates the number of LLS's with $N_{HI} \geq 10^{17.5}\, cm^{-2}$ by a factor 2. The middle panel of Fig. 1 shows why this is: these higher column density LLS actually contribute little to λ_{eff}.

We venture that scatter in the density distribution around haloes may be the main culprit for the underestimate in dN/dX in the model. Indeed, these higher column density systems have by construction an optical depth to ionizing photons of around unity. Consequently, a small increase in total column density may result in an exponential increase in neutral column density due to the onset of self-shielding. The impact of such *scatter* on the CDDF is substantial: a 0.2 dex Gaussian scatter in $\log N_{HI}$ results in a factor of 2 increase in dN/dX – enough to bring the model in good agreement with the data. Importantly, this exponential dependence on column density mostly affects absorbers around the knee of the CDDF, where the absorbers transition from optically thin to optically thick.

APPENDIX C: STATISTICS OF τ_{EFF}

In this Appendix, we derive an approximate analytical expression for the PDF of τ_{eff}, as discussed in Section 3.3. Our derivation goes as follows. At sufficiently low N_{HI}, the mean number of lines that contribute to τ_{eff} may be large enough that the central limit theorem is applicable. In that case, the lines are approximately Gaussian distributed (with mean $\langle N \rangle$ and dispersion $\langle N \rangle$). Integrating over dN_{HI}, and integrating over dX then corresponds to summing over independently distributed Gaussian variables. Therefore, the sum is

also Gaussian distributed, with mean the sum of the means, and dispersion the sum of the dispersions. We will denote the value of τ_{eff} due to these low column-density lines by $\tau_{eff,\,low}$, and its PDF is therefore

$$\mathcal{P}_G(\tau_{eff,low}|\mu, \sigma) = \frac{1}{(2\pi\sigma^2)^{1/2}} \exp\left(-\frac{(\tau_{eff,low} - \mu)^2}{2\sigma^2}\right)$$

$$\mu(X) = X \int_0^{N_{HI,low}} f(N_{HI})(1 - \exp(-\tau))dN_{HI}$$

$$\sigma^2(X) = X \int_0^{N_{HI,low}} f(N_{HI})(1 - \exp(-\tau))^2 dN_{HI}. \quad (C1)$$

We added a subscript 'G' as a reminder that we assume Gaussian statistics.

We can account for the higher column density absorbers as follows. Let's take $N_{HI,low} = 10^{17.2}\, cm^{-2}$. In that case, the weighting factor $(1 - \exp(-\tau)) \approx 1$ for those lines with $N_{HI} \geq N_{HI,\,low}$. The PDF due to these higher column density lines is now a sum of independently distributed Poisson variables, hence also a Poisson distributed variable.[19] Denoting the value of τ_{eff} due to these high column-density lines by $\tau_{eff,high}$, we find that its PDF is given by

$$\mathcal{P}_P(\tau_{eff,High}) = \mathbb{P}(N|N_P)$$

$$N_P(X) = X \int_{N_{N_{HI,low}}}^{\infty} dN_{HI}, \quad (C2)$$

with subscript 'P' as a reminder that we assume Poisson statistics.

The total effective optical depth is $\tau_{eff,low} + \tau_{eff,high}$, with PDF

$$\mathcal{P}(\tau_{eff}(X)) = \sum_{N=0}^{\infty} \mathbb{P}(N|N_P)\mathcal{P}_G(\tau_{eff} - N|\mu, \sigma), \quad (C3)$$

with μ, σ, and N_P all proportional to X. The mean of this distribution is the sum of the means of $\tau_{eff,low}$ and $\tau_{eff,high}$,

$$\langle \tau_{eff}(X; z) \rangle = X \int_0^1 f(N_{HI})\left[1 - \exp(-\tau)\right]dN_{HI}$$

$$+ X \int_1^{\infty} f(N_{HI})dN_{HI}$$

$$\approx 4.2\, X\, \frac{f_{17.2}(z)}{\sigma_{th}}, \quad (C4)$$

where we used the power-law approximation to the CDDF of equation (13). The numerical value also shows the limitation of setting $1 - \exp(-\tau) \to 1$ for the high column density absorbers. If we had not made that approximation, then $\langle \tau_{eff}(X; z) \rangle = 4.02\, X\, f_{17.2}(z)/\sigma_{th}$.

We can now compute the PDF of the co-moving attenuation length – *i.e.* the PDF of X where $\tau_{eff} = 1$ – as follows. The fraction of sight lines that reach $\tau_{eff} > 1$ for a given value of X is

$$\mathcal{P}(\tau_{eff} > 1|X) = \int_1^{\infty} \mathcal{P}(\tau_{eff}|X)d\tau_{eff}$$

$$= \frac{1}{2} \sum_{N=0}^{\infty} \mathbb{P}(N|N_P)\{1 \pm Erf(x)\}$$

$$x \equiv \frac{1 - N - \mu}{(2\sigma^2)^{1/2}}. \quad (C5)$$

Here, Erf denotes the error function, and the upper and lower signs applies to the case where x is negative or positive. The fraction of

---

[19] The reason this works in this approximation is that the weights of each individual Poisson variable are now equal, $1 - \exp(-\tau) \to 1$, so now it is a sum rather than a more general linear combination of Poisson variables.

paths that reach τ_{eff} between X and $X + \mathrm{d}X$ follows by taking the derivative with respect to X,

$$
\begin{aligned}
\mathcal{P}(\tau_{\mathrm{eff}} = 1, X) &= \frac{\mathrm{d}\mathcal{P}(\tau_{\mathrm{eff}} > 1 | X)}{\mathrm{d}X} \\
&= \sum_{N=0}^{\infty} \left\{ \left(\frac{N}{N_P} - 1 \right) \mathbb{P}(N|N_P) \left\{ 1 \pm \mathrm{Erf}(\mp x) \right\} \frac{N_P}{X} \right. \\
&\quad + \left. \mathbb{P}(N|N_P) \frac{\exp(-x^2)}{\pi^{1/2}} \left(\frac{x}{2X} + \frac{\mu_G}{(2\sigma^2)^{1/2}X} \right) \right\}.
\end{aligned}
$$

(C6)

This is the approximate analytical expression for the probability distribution of the attenuation length that we set out to obtain.

This paper has been typeset from a TeX/LaTeX file prepared by the author.